iScience

CellPress
OPEN ACCESS

Article

C19MC drives nucleolar invasion of mitochondria and meiotic nuclear division in human cancers

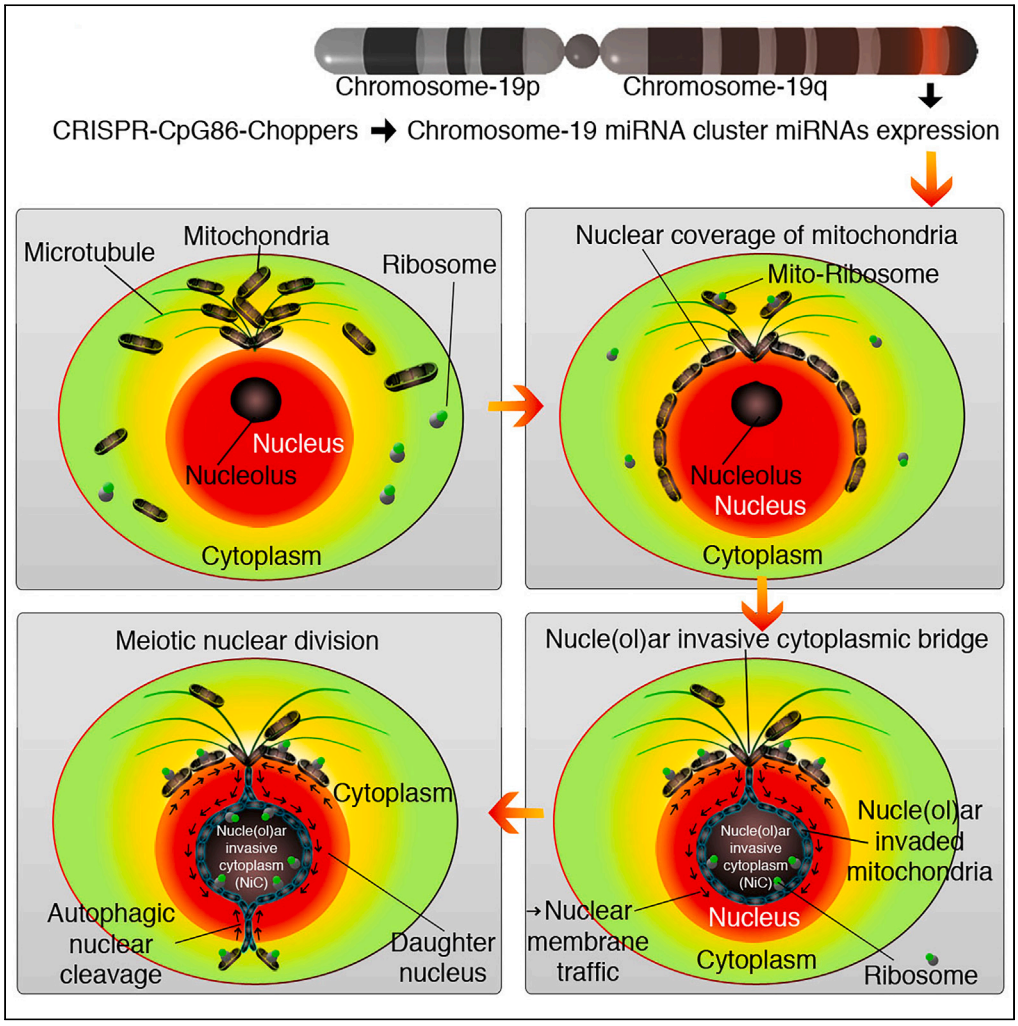

Goodwin G. Jinesh, Marian T. Smallin, Nino Mtchedlidze, Marco Napoli, John H. Lockhart, Elsa R. Flores, Andrew S. Brohl

goodwinjinesh@gmail.com (G.G.J.)
andrew.brohl@moffitt.org (A.S.B.)

Highlights

C19MC drives the nucle(ol)ar invasion of cytoplasm and meiotic nuclear division

Mitochondria, RPS6, nucleolin and REST are the cargos that invade nucle(ol)us

Aurora-B, rDNA expression, and CDK1 regulate nucle(ol)ar invasion of cytoplasm

C19MC drives nuclear coverage of mitochondria for nucle(ol)ar invasion

Jinesh et al., iScience 27, 111132
November 15, 2024 Published by Elsevier Inc.
https://doi.org/10.1016/j.isci.2024.111132

iScience

CellPress
OPEN ACCESS

Article

C19MC drives nucleolar invasion of mitochondria and meiotic nuclear division in human cancers

Goodwin G. Jinesh,[1,2,5,*] Marian T. Smallin,[1,2] Nino Mtchedlidze,[1,2] Marco Napoli,[1] John H. Lockhart,[1] Elsa R. Flores,[1,3] and Andrew S. Brohl[2,4,*]

SUMMARY

The chromosome-19 miRNA cluster (C19MC) restricts viruses depending on the multinucleated state of placental trophoblasts. However, the relationship of C19MC to multinucleation is unknown. Here we show that C19MC is coexpressed in multiple cancer type subsets with meiosis-related genes. We discovered a novel meiosis-III that exhibits simultaneous progression of meiotic nuclear division (MND) and cytokinesis. C19MC promotes meiotic bridged-chromosomes to block MND and cytokinesis to generate multinucleated cells. MND starts with the invagination of nuclear membrane to form nucle(ol)ar invasive cytoplasm (NiC), mitochondria and protein cargoes. Aurora-B regulates the efflux of cargos from NiC, whereas C19MC, CDK1, and autophagy promote cargo influx to inflate NiC size for MND progression. Using CRISPR human genetic engineering we demonstrate that the C19MC expression is required for NiC-driven MND and multinucleation. This discovery has impacts on cancer-pathogen interactions, immunotherapy, vertical transmission of viruses, antiviral research and SpCas9-CRISPR therapeutics.

INTRODUCTION

Vertical transmission of viruses across the placenta (at the interface between fetus and mother) is restricted by the multinucleated placental syncytiotrophoblasts but not by the mononucleated cytotrophoblasts.[1,2] C19MC is an antiviral response miRNA cluster[2,3] with 46 highly similar but distinct miRNAs[4,5] that are expressed primarily in the placenta.[5] However, it is not known whether the cells acquire multinucleation status because of viral proteins or due to C19MC. In cancers, multinucleated as well as giant nucleated, spheroid-forming poorly differentiated cells with chromosomal instability are considered tumorigenic stem cells.[6–12] Interestingly, two rare pediatric cancer types, undifferentiated embryonal sarcoma of the liver (UESL)[13] and embryonal tumors with multilayered rosettes (ETMRs) of the brain,[14] overexpress C19MC that is associated with chromosomal translocation assisted fusion of C19MC with other genes such as ZIM2/PEG3[13] or TTYH1.[14] However, the genetic switch that regulates C19MC expression remains elusive. While we previously investigated C19MC expression in triple-negative breast cancer[15] and hepatocellular carcinoma,[16,17] we comprehensively examined The Cancer Genome Atlas (TCGA) data in this study to get insights into the function and regulation of C19MC in human cancers. We identify and validate the meiotic nuclear division (MND)-related gene expression signatures of C19MC^{High} cancers *in vitro* using CRISPR human genetic engineering. Our findings on the novel MND might in future translate to restricting viruses inside cells, cancer immunotherapy, and vertical transmission of viruses across human/primate placenta.

RESULTS

A novel meiosis-III and meiotic gene expression signature in C19MC^{High} cancers

C19MC is overexpressed in subsets of tumors from multiple cancer types in TCGA database, with the maximum expression in testicular germ cell tumors (TGCTs). We focused on 20 cancer types that allow sufficient C19MC^{High} and C19MC^{Low} group stratification (Figure 1A). Gene set enrichment analysis (GSEA) revealed a strong and coherent enrichment of meiosis-related gene signatures in C19MC^{High} tumors (Figure 1B). Considering the fact that TGCTs are at the site of germline meiosis, we first asked if meiosis can happen in non-germline cells. Interrogation of meiosis gene signature in EnrichR pointed to the MCF-7 breast cancer cells (Figure S1A). In MCF-7 cells we found that chromosomes condense and anchor from the interior of the nucleus toward the nuclear membrane, and that the nucleus undergoes reduction division with a dumb bell shape created by nuclear cleavage furrow (NCF) (Figure 1C). In addition, we found a novel "meiosis-III," where the reduction nuclear division (analogous to meiosis-I) and cytokinesis (analogous to meiosis-II) progress simultaneously. In normal meiosis these events are

[1]Department of Molecular Oncology, H. Lee Moffitt Cancer Center & Research Institute, Tampa, FL 33612, USA
[2]Molecular Medicine Program, H. Lee Moffitt Cancer Center & Research Institute, Tampa, FL 33612, USA
[3]Cancer Biology and Evolution Program, H. Lee Moffitt Cancer Center & Research Institute, Tampa, FL 33612, USA
[4]Sarcoma Department, H. Lee Moffitt Cancer Center & Research Institute, Tampa, FL 33612, USA
[5]Lead contact
*Correspondence: goodwinjinesh@gmail.com (G.G.J.), andrew.brohl@moffitt.org (A.S.B.)
https://doi.org/10.1016/j.isci.2024.111132

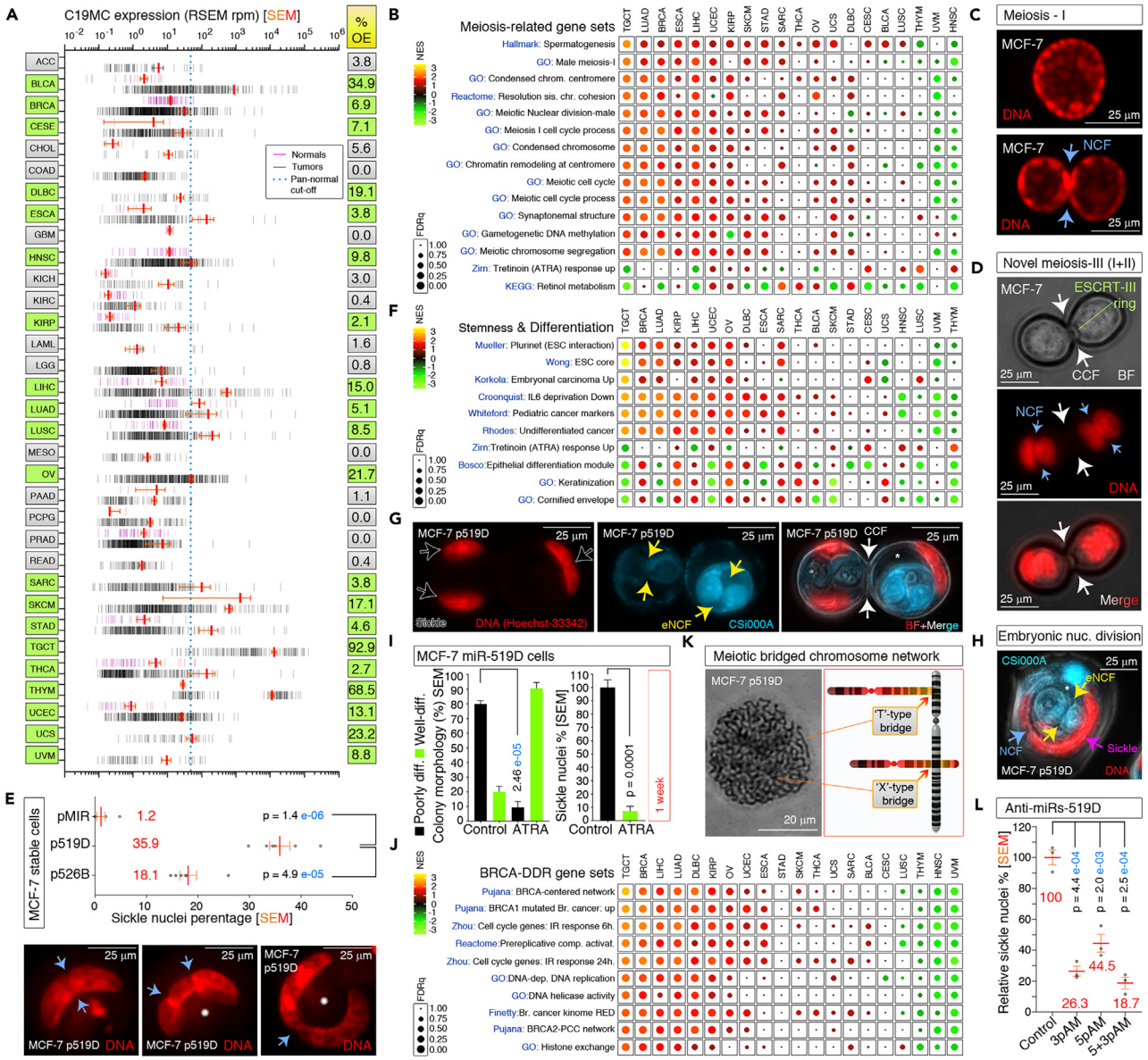

Figure 1. C19MC miRNAs promote embryonic stemness and interfere with meiotic nuclear division through meiotic bridged chromosomes

(A) Cumulative C19MC expression across various cancer types in TCGA dataset. Percentage of tumors that overexpress C19MC beyond the pan-normal cut-off (dotted line) is indicated on right.

(B, F, and J) Green-shaded cancer types in (A) were further subjected to C19MC$^{High/Low}$ GSEA differential gene expression in (B), (F) and (J) where a meiotic (excluding mitotic), ESC, DNA damage response (DDR) enrichments were grouped respectively.

(C) Rare meiotic figures in MCF-7 cells where chromosomes condensed toward nuclear membrane.

(D) A novel type of meiosis-III with nuclear cleavage furrow (NCF) and cytokinesis cleavage furrow (CCF) with ESCRT ring at different planes.

(E) Sickle nuclei count in C19MC miRNA overexpressed MCF-7 cells. Note the aberrant DNA accumulation at nuclear cleavage furrows (Blue arrows); *Nucleolus.

(G and H) Embryonic nuclear division visualized with Cy5-CSi000A probe (G and H). *Vacuole.

(I) C19MC-induced poor differentiation status is reversible by ATRA.

(K) Meiotic bridged chromosomes (MBCs) efficiently generated by miR-519D (please see Figures S1L and S1M).

(L) Anti-miR-519D reverses sickle nuclear phenotype in MCF-7 miR-519D stable cells to show specificity.

marked into two sequential divisions: meiotic reduction division-I, and then chromosome duplication and a mitosis-like division-II. As this cell division exhibits the features of both meiosis-I and II simultaneously, we coined the term meiosis-III (Figure 1D). Notably, meiosis-III did not display discrete chromosome condensation but displayed diffuse type irregular DNA condensation. Therefore, meiosis can happen in non-germline cells.

Overexpression of individual C19MC miRNAs in MCF-7 cells, especially miR-519D dented the meiotic nuclear shape to a sickle shape with multi-plane nuclear cleavage furrows in it (Figure 1E). Such sickle nucleated meiosis-III physiologically happens in C19MC^{High} human breast cancer, and at *in vitro* the cytokinetic ESCRT cut results in binucleated daughter cells with one sickle nucleus and another nucleus with or without chromosome condensation (Figures S1B and S1C). Stimulation of endogenous C19MC miRNAs by zinc metal response also promotes sickle nuclei (Figures S1D and S1E). We next examined the expression of meiosis specific protein in C19MC miRNA overexpressed cells to confirm the influence of C19MC miRNAs in meiosis. We chose *SYCP2* because its mRNA was enriched in C19MC^{High} meiosis-related gene signatures. The translated product of *SYCP2*, the meiotic synaptonemal complex protein-2, was promoted more by miR-519D than miR-526B (Figure S1F), suggesting that miR-519D has a prominent role in meiosis.

C19MC miR-519D promotes undifferentiated ESC state with MND and END during meiosis-III

Among all GSEA enrichments in C19MC^{High} tumors, TGCT exhibited the embryonic stem cell (ESC) signature as the top candidate, which is accompanied by undifferentiated cancer, interleukin-6 (IL-6) inflammatory, embryonal carcinoma, and pediatric cancer marker signatures in addition to multiple cancer types (Figure 1F). Using a mitochondria-labeling RNA probe Cy5-CSi000A (Figure S1G), we detected embryonic nuclear division (END) with embryonic nuclear cleavage furrow (eNCF) in meiosis-III in MCF-7 miR-519D overexpressing cells (Figures 1G and 1H). Notably, MND (detected by Hoechst-33342 positive DNA) and END (detected by Cy5-CSi000A probe) progress within the same cell exhibiting meiosis-III (Figures 1G, 1H, and S1I). This nuclear DNA labeling by Cy5-CSi000A is potentially due to entosis (cell inside cell) and the subsequent mixture of mitochondria and nuclear genomes, as the END is always observed within vacuolar structures of the MCF-7 miR-519D cells and in the C19MC^{High} breast cancers (Figures 1G, 1H, and S1H–S1J). Furthermore, 80–90% of the MCF-7 miR-519D overexpressed cells exhibited sickle nuclei and undifferentiated morphology that are reversed back to differentiated and sickle nuclei depleted states upon induction with all-*trans* retinoic acid (ATRA, a meiotic promoter in male germ cells[18]) (Figures S1K and 1I). Therefore, we inferred that miR-519D delayed the MND to keep the cells in undifferentiated state and that the meiotic promoter ATRA overcomes the delay.

Meiotic bridged-chromosomes block meiotic nuclear reduction division by generating mini nuclei and chromosomal instability

As per the GSEA results, C19MC^{High} tumors also displayed enrichments of BRCA-centered DNA damage response gene sets (Figure 1J). The nuclear cleavage furrows in MCF-7 519D sickle nucleated cells usually exhibited tangled DNA condensates (Figure 1E). Isolation of meiotic nuclei and subjecting it to cytogenetics has revealed that meiotic bridged-chromosome (MBC) network (Figures 1K and S1L) and chromosome-cohesion resolution defects such as anaphase bridge (Figure S1L) interfere with the MND, to potentially activate the "NoCut checkpoint."[19,20] To confirm this, we isolated meiosis-III nuclei from MCF-7 miR-519D overexpressed cells and observed the meiosis-III nuclei in a bridged fashion where the meiotic bridged-chromosomes accumulate as bridged mini nuclei in between the large "supposed to be" daughter nuclei (Figure S1M). Of note, meiotic bridged mini nuclei are different from micronuclei, as mini nuclei do have bridges to the main nuclei. Interestingly, MBCs and non-MBCs segregate during MND (Figure S1M). While MBCs demonstrated structural chromosomal instability (sCIN) and posed difficulty in counting chromosome numbers, we evaluated the numerical chromosomal instability (nCIN) in cells that lack MBCs. Following 2 months of maintenance, the MCF-7 miR-519D cells gained ~5 chromosomes on average (Figure S1N). To gain insight on the genomic content reduction nature of the MND, we measured the Hoechst-33342 positive DNA content of individual nuclei despite these nuclei may remain within the same mother cell. We found that the MND in miR-519D overexpressed MCF-7 cells indeed had halved the DNA content on average (Figure S1O). Therefore, MBCs prevent cytokinesis so as to retain the daughter nuclei within the mother cells often with a sickle shape (Figures 1E and S1M). Usage of anti-miR-519D in miR-519D overexpressed MCF-7 cells significantly inhibited sickle nuclei formation (Figure 1L), suggesting the role of miR-519D in MBC formation. Therefore, C19MC utilizes DNA damage response to generate MBCs to hamper the progression of MND through activation of the NoCut checkpoint and generate multinucleated cells with structural chromosomal instability (sCIN) and numerical chromosomal instability (nCIN).

Meiotic nuclear division begins with nucle(ol)ar invasion of cytoplasm

GSEA results of 20 different C19MC^{High} cancer types revealed a strong upregulation of influenza and HIV infection gene signatures in C19MC^{High} TGCTs, in addition to other viral inducible gene signatures across various cancer types (Figure S2A). The influenza and HIV infection signatures comprise genes regulating rDNA transcription, rDNA translation, proteasome, nucleoporins, and nuclear import/export. Of these, the rDNA-influenza signature (RPL and RPS genes) is upregulated in all 1,020 Cancer Cell Line Encyclopedia (CCLE) cell lines (Figure S2B). A search for influenza signature pointed to the WM793 melanoma cell line, which has high cluster-wide C19MC expression based on CCLE next generation sequencing (NGS) data, and our further verification by RT-qPCR (Figures S2C–S2F). Having baseline hyper-C19MC expression, WM793 cells exhibited spontaneous sickle nuclei, MND (Figure 2A), nuclear membrane margination of condensed chromosomes, and meiotic bridged-chromosomes at nuclear cleavage furrows (Figure S2G). TCGA GSEA data on C19MC^{High} cancers also revealed that a strong enrichment of Aurora-B and anaphase promoting complex (APC)-related gene signatures but without any enrichments on ESCRT[20] signature (Figures S2H and 2B). These results suggested a major role for Aurora-B and NoCut checkpoint in the process of multinucleation by disabling cytokinesis.

Inhibition of Aurora-B in WM793 cells resulted in the formation of "Hoechst-33342 stained DNA negative" sub-domains/compartments within nuclei in 58% of the cells, which we termed as nucle(ol)ar invasive cytoplasm (NiC) (Figure 2C) based on the results of following experiments in this study. This compartment is formed by the invagination/self-invasion of nuclear membrane as visualized by EGFP-emerin (marks

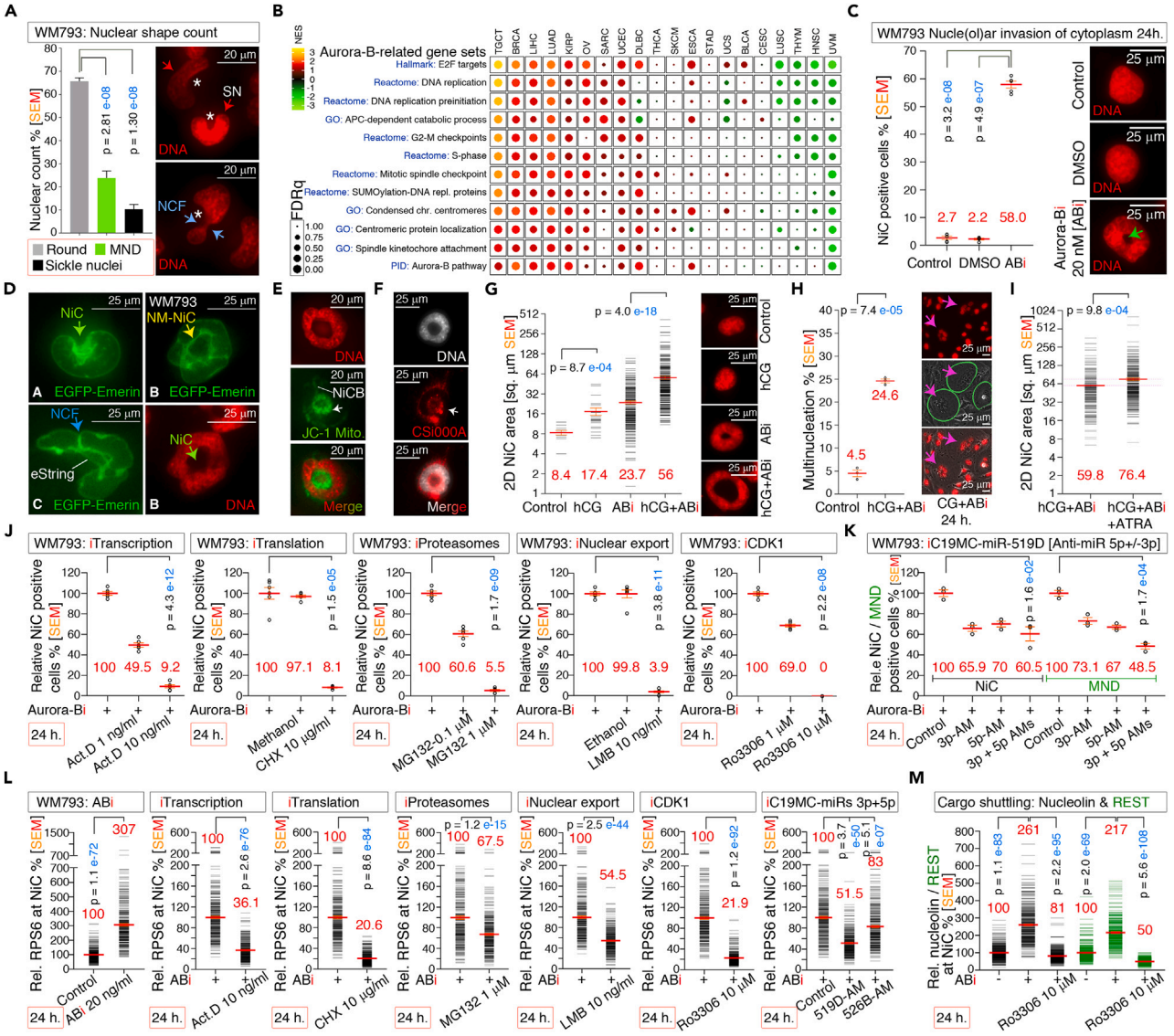

Figure 2. Nucle(ol)ar invasion of cytoplasm (RPS6, nucleolin, REST, and mitochondria) leads to meiotic nuclear division (MND)

(A) Baseline sickle nuclei (red arrow) and MND percentages in C19MC^{High} cell line WM793 (nuclear cleavage furrow [NCF], blue arrows; DNA, Hoechst-33342 live stained).

(B) GSEA enrichments in 20 TCGA C19MC^{High} cancer types showing Aurora-B-related gene signatures.

(C) Aurora-B inhibition results in nucle(ol)ar invasive cytoplasm (NiC, green arrow).

(D–F) EGFP-emerin labeled nuclear membrane showing NiC process (sub-panel-A within D) to form a nuclear membrane bound nucle(ol)ar invasive cytoplasmic compartment (NM-NiC, sub-panel-B) and emerin strings (eStrings) that hold the sickle nuclear shape upon opening-up of the nucle(ol)ar invasive cytoplasmic compartment (sub-panel-C). Localization of mitochondria using JC-1 staining (E) and using Cy5-CSi000A RNA probe (F) within NiC. A nucle(ol)ar invasive cytoplasmic bridge (NiCB) is indicated in (E). Please see Figures S3G and S4B for schematic details on NiCB.

(G and H) Meiotic promoter hCG promotes the size of NiC and multinucleation in WM793 cells.

(I) Meiotic promoter ATRA enhances the size of NiC promoted by hCG in WM793 cells.

(J) Ribosomal biogenesis/rDNA pathway (HIV+IAV-signatures) inhibitors impede NiC formation (please see Figure S2N to see why CDK1 inhibitor was used).

(K) Inhibition of C19MC miRs with anti-miR-519D impedes NiC and MND frequency (anti-C19MC-miRs were transiently transfected to check the C19MC dependency).

(L and M) Immunofluorescence and ImageJ quantification of protein cargo traffic (RPS6, nucleolin, and REST/NRSF) into the nucle(ol)ar invasive cytoplasmic compartment (Please see Figure S2L to see immunolocalization into the NiC).

the inner nuclear membrane[21,22]) (Figure 2D), and NiC encloses mitochondria as visualized with JC1 staining and independently with an RNA probe, Cy5-CSi000A (Figures 2E and 2F). Cells generally form a single NiC per nucleus but frequently double NiC are formed in WM793 cells (Figure S2I). We detected NiC in WM793 cells undergoing MND, by arresting the cells using nocodazole to collect dividing cells and then replacing the nocodazole with Aurora-B inhibitor containing medium to mimic NoCut checkpoint by arresting cytokinesis (Figure S2J). We also found that the NiC is a closed compartment that encloses "Giemsa positive DNA" but lacks "Hoechst-33342 positive DNA" as shown in hypotonic salt isolated nuclei (Figure S2K). Presence of Giemsa positive DNA at NiC raised the possibility that the NiC could be nucleolus that was engulfed by the invading nuclear membrane. We found that nucleolin (nucleolus marker), RPS6 (ribosomal constituent regulating spermatogenesis[23] that can go to nucleolus for assembly) and REST accumulate within the NiC (Figure S2L). Therefore, we conclude that the NiC is a nuclear membrane guarded nucle(ol)ar cytoplasmic hybrid compartment (nucleoli are not usually bound by membranes[24]) that encloses cytoplasmic materials such as mitochondria, proteins, and possibly ribosomes (ribosomes are usually assembled at nucleoli[24,25] and can enter into NiC as mitochondrial ribosomes).

C19MC, meiotic regulators, and rDNA expression determine the size of NiC

Considering the fact that influenza A virus (IAV) and human immunodeficiency virus (HIV-1) localize to a large nuclear sub-domain positive for nucleolar markers,[26] and the IAV+HIV infection signatures (Figure S2B) matched to the meiotic gene signature in C19MC^{High} tumors (Figure 1B), we examined the relationship of NiC to meiotic regulators. We compared the top two C19MC expressing cancer types (TGCT: germ line site and THYM: non-germ line site) to find any enrichment of meiotic regulators. The pregnancy hormone human chorionic gonadotrophin (hCG)-A and -B RNAs are consistently promoted in C19MC^{High} tumors (Figure S2M) and hCG is also a known meiotic promoter.[27] Interestingly, treatment of WM793 cells with either hCG alone or in combination with Aurora-B inhibitor increased the size of NiC and raised the frequency of multinucleated cells (Figures 2G and 2H). Furthermore, combination of a chemical promoter of meiosis (ATRA),[28] with hCG further enlarged the size of NiC in the presence of Aurora-B inhibitor (Figure 2I). Therefore, NiC is relevant to multinucleation and is regulated by meiotic promoters.

We found that inhibitions of ribosome biogenesis/rDNA pathway[25] (combined IAV and HIV signatures) at any level (inhibitions of general transcription, translation, proteasomes, nuclear export/import, or CDK-1) block the formation of NiC (Figures 2J and S2N, and S2O). Likewise, interfering C19MC with anti-miRs impeded nucle(ol)ar invasion of cytoplasm and MND (Figures 2K and S2P).

Therefore, C19MC regulates nucle(ol)ar invasion of cytoplasm and multinucleation through hCG, ATRA, rDNA, and Aurora-B pathways.

RPS6, REST, and nucleolin are protein cargoes of NiC

Although Giemsa positive DNA is localized within NiC (Figure S2K), we anticipated a cargo traffic between the NiC and cytoplasm/nucleus would determine its size. We found that ribosomal small subunit protein RPS6 localizes and accumulates ~200% more at the NiC when Aurora-B is inhibited in WM793 cells, and this accumulation was blocked by rDNA pathway inhibitors or by a CDK-1 inhibitor (Figure 2L). Similarly, nucleolin and REST/NRSF were also trafficked inside and outside of the NiC upon inhibition of Aurora-B with or without CDK-1 inhibitor (Figure 2M). Therefore, it is conceivable that CDK1 regulates the cargo influx and Aurora-B regulates the cargo efflux at NiC. Anti-miR usage against C19MC miRNAs in WM793 cells further reiterated that this protein traffic at NiC is C19MC-dependent (Figures 2L and 2K). Notably, the data from chemical inhibitors are more robust compared to the anti-C19MC-miR data. Therefore, we aimed for a robust genetic C19MC targeting approach to further validate these data.

CpG-island-86 (CpG86) regulates C19MC miRNA expression to activate proteasome

To understand the C19MC expression, we sought to CRISPR engineer the genome at C19MC landscape. C19MC^{High} expressing cells and C19MC^{High} TGCTs show a potential transcription start at the C19MC upstream CpG86 (Figure S3A). CpG86 has 13 specific repeats (Figure 3A) and this repeat region exhibits hypervariability across 19 cell lines examined, with the lowest repeat number in MCF-7 cells (missing 8-repeats naturally) (Figures S3B and S3C). We generated two CRISPR-CpG86-chopper guide-RNA constructs (using the SpCas9 system[29]). Both chopper guide RNAs are capable of collectively targeting 16 unique sites within the CpG86 13-repeat region (Figure 3A). We CRISPR knocked-out 10 out of 13 repeats within CpG86 in WM793 cells using the CpG86-chopper guide-RNA constructs (Figures 3A and S3B, and S3C). Interestingly, the SpCas9 control construct (NGP) suppressed C19MC miRNA expression by ~95%, whereas the CRISPR-CpG86-chopper constructs restored the C19MC expression (Figure 3A). A deeper examination revealed that both WM793-NGP control and WM793-choppers pooled cells (Chop. P) have SpCas9 integrated in the genome and expressed SpCas9 at the transcript level. However, SpCas9 protein is expressed only in NGP control, but it was degraded by proteasome in CRISPR-CpG86-choppers transfected cells (Figures 3B and 3C). Inhibiting proteasome but not autophagy resulted in the accumulation of potentially ubiquitinated SpCas9 protein of >500 kDa (Figure 3C) at the perinuclear region (Figure S3E). Of note, SpCas9 is known for multi-site ubiquitination to generate similar higher molecular weight (HMW) band.[30] Therefore, the CpG86 hypervariable 13-repeats act as the genomic switch for C19MC repression by SpCas9, and the C19MC-directed ubiquitin proteasome activation degrades SpCas9 to overcome the repression at CpG86. Consistently, proteasome gene signatures are enriched in multiple C19MC^{High} TCGA cancer types, and SpCas9 in choppers cells accumulated at the perinuclear region predominantly and at NiC to a lesser extent when proteasomes were inhibited (Figures S3D and S3E). We evaluated the meiotic synaptonemal complex protein-2 (SYCP2) in these CRISPR-engineered cells and found that SpCas9 indeed suppressed SYCP2 but choppers restored it (Figure 3D).

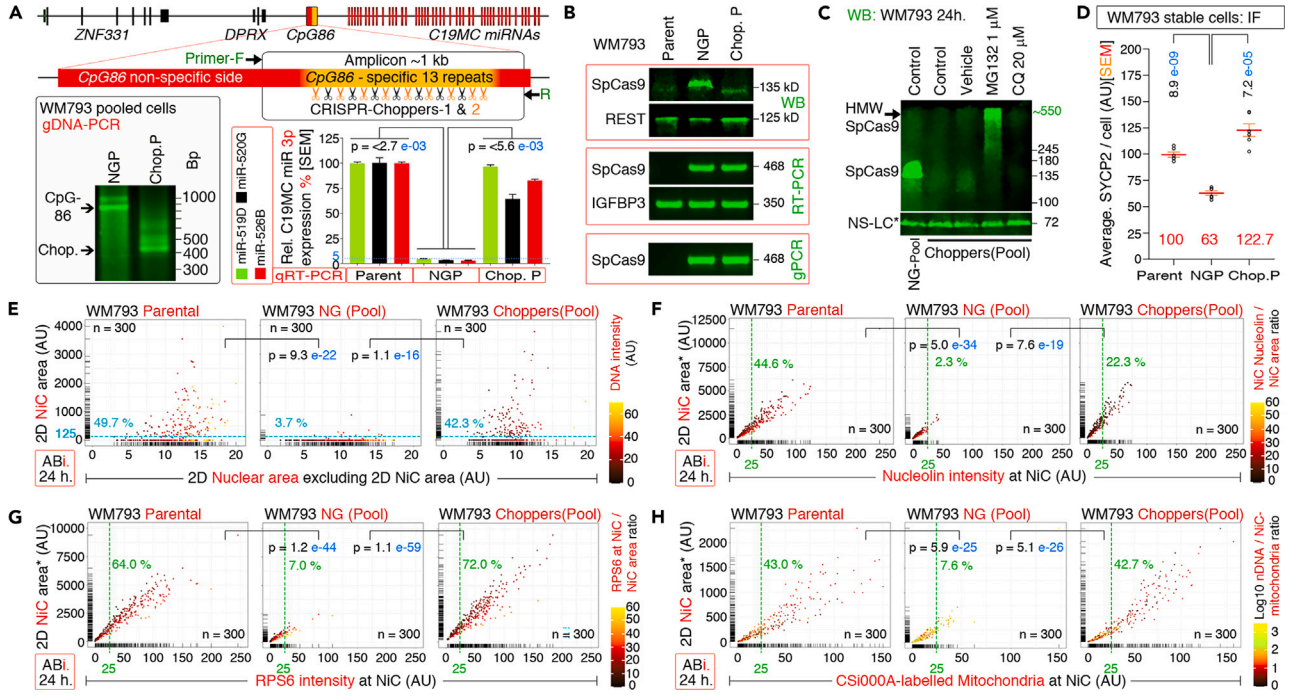

Figure 3. CpG86-regulated C19MC miRNAs are required for nucle(ol)ar invasive cytoplasm (NiC), and protein and mitochondria cargo traffic into NiC

(A) CRISPR strategy to knock-out 13-repeats within C19MC upstream CpG86. Arrows indicate the screening primer locations and directionality (F/R, forward/reverse). Bottom left inset: Choppers pooled WM793 cells (Chop. P) showing the CRISPR knockout of CpG86 repeats (please see Figure S3C for Sanger sequencing confirmation). Bottom right inset: RT-qPCR evaluation of C19MC miRNA expressions in CRISPR-engineered cells. NGP: SpCas9 control pooled WM793 cells.

(B) Evaluation of SpCas9 at genomic, transcription, and protein levels by PCR, RT-PCR, and western immunoblotting, respectively.

(C) CRISPR-choppers-1 and 2 degrade SpCas9 through proteasomes as evaluated by western immunoblotting with MG-132. *Non-specific band from a different re-probing antibody is used as loading control.

(D) Immunofluorescence quantification showing the suppression of meiotic SYCP2 levels by SpCas9 and its restoration by choppers.

(E) SpCas9 suppresses NiC formation and CRISPR-choppers restores it, Blue horizontal dotted line is a gate to calculate the percentage (given in blue font) of large NiC positive cells.

(F–H) Immunofluorescence quantification of protein cargos nucleolin (F), RPS6 (G), and Cy5-CSi000A staining and quantification of organelle cargo mitochondria (H) in CRISPR engineered cells to show the C19MC dependence of cargo traffic into the nucle(ol)ar invasive cytoplasmic compartment as evaluated under Aurora-B inhibited conditions. Vertical green dotted lines are gates used to calculate the percentage (indicated in green fonts) difference in traffic between cell types. nDNA, nuclear DNA; AU, arbitrary units scaled down; *n* = 300 data points from replicates. See Figures S3F and S3G for schematics on protein vs. organelle traffic into the nucle(ol)ar invasive cytoplasmic compartment.

C19MC drives nucle(ol)ar invasion of cytoplasm and cargo traffic

To understand the cause-effect relationship between C19MC and cargo traffic into and out of NiC, we utilized the pooled CRISPR-engineered cells. SpCas9 in NGP cells (which suppresses C19MC miRNA expression) blocked the formation of NiC by >90%, and NiC influx of RPS6 and nucleolin were suppressed to a similar extent upon Aurora-B inhibition (Figures 3E–3G). Conversely, CRISPR-choppers (which restore C19MC miRNA expression) restored the formation of NiC by >90%, and NiC-influx of RPS6 and nucleolin were restored to a similar extent upon Aurora-B inhibition (Figures 3E–3G). Therefore, the influx and efflux of protein cargos are dependent on C19MC and might also happen through nuclear pore complexes (NPCs) as nucleolin and ribosomal proteins are known to undergo nuclear-cytoplasmic transport through NPCs.[31]

C19MC drives mitochondria traffic into the NiC

While a nuclear pore complex (NPC) through traffic is known for protein complexes to enter the nucleus and subsequently into the nucleolus, it cannot explain organelle influx into the NiC such as mitochondria and potentially ribosomes (as RPS6 immunoreactivity could also include assembled ribosomes). Therefore, we hypothesized that a microtubule-organizing center (MTOC)-dependent traffic and push of cytoplasmic materials such as mitochondria into the nucle(ol)us could be the cause. Immunofluorescence for β-tubulin demonstrated that MTOC invades NiC in a small subset of ~5% cells, but the remaining cells lacked β-tubulin expression (Figures S3F and S3G). Mitochondria traffic into the NiC was suppressed >80% in SpCas9 controls cells whereas it was restored by choppers under Aurora-B inhibited conditions (Figure 3H), demonstrating that the mitochondria cargo influx and efflux into the NiC is also C19MC-dependent. Therefore, a CRISPR genetic engineering approach further confirmed the C19MC-directed NiC formation and organelle cargo traffic into it.

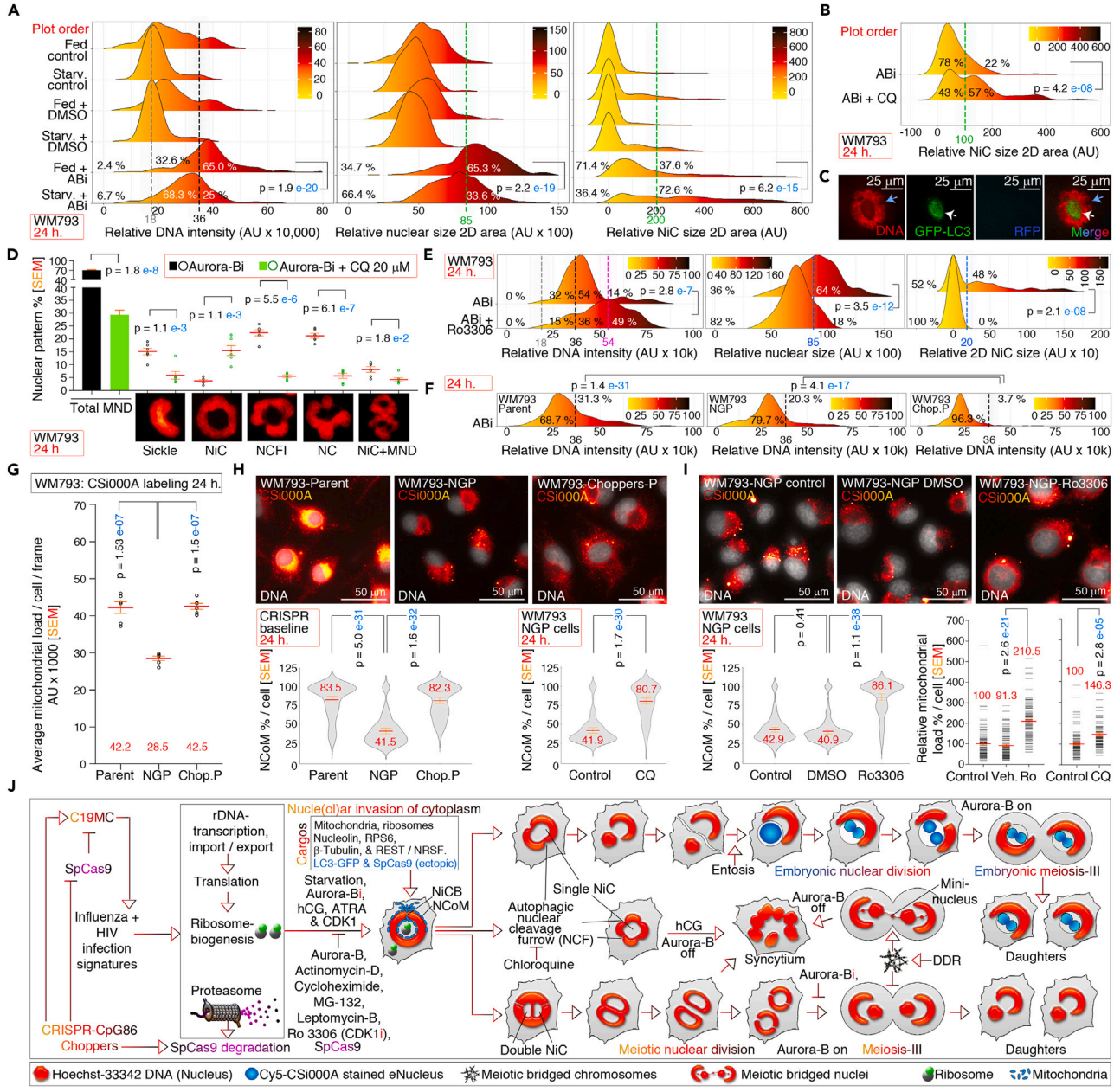

Figure 4. C19MC miRNAs and autophagy direct nuclear coverage of mitochondria (NCoM) and meiotic nuclear cleavage furrow (NCF) ingression

(A) Starvation-induced autophagy doubles the size of nucle(ol)ar invasive cytoplasm (NiC) while impairing DNA synthesis in WM793 cells. AU, scaled down arbitrary units. Gray dotted line: G_1 stage, and black dotted dine G_2 stage of the cell cycle.

(B) Autophagy inhibition augments the NiC size under fed conditions. Only NiC forming cells were measured. Green dotted line: discriminatory gate for percentage calculations.

(C) Autophagic flux within subcellular locations under Aurora-B inhibited condition: NiC is an autophagy immune zone as GFP-LC3 accumulate at NiC but degraded at cytoplasm. See Figure S4A for cytoplasmic/perinuclear GFP-LC3.

(D) Autophagy drives NCF ingression from the cytoplasmic side. Total meiotic nuclear division (MND) is shown as bars and sub-types as data points. NiC is without any NCF ingression, NCFI is NiC with NCF ingression, NC is with nuclear cleavage that opened up at least at one point, NiC+ MND is dual NiC with NCF.

(E) NiC inhibition by CDK1 inhibitor promotes DNA synthesis to a triploid content (purple dotted line).

(F) Baseline DNA intensity levels between CRISPR-engineered and not engineered cell types. Black dotted line, diploid level.

(G) Cy5-CSi000A labeling and quantification of mitochondrial load/cell in CpG86-CRISPR-engineered WM793 cells.

(H and I) Baseline and NiC altering drug-induced changes in nuclear coverage of mitochondria (NCoM: violin plots). Relative mitochondrial load/cell was displayed in aligned dot plots. CQ, chloroquine. See Figure S4B for a schematic depicting how NCoM helps passive mitochondria and potentially mitochondrial ribosome traffic into the nucle(ol)ar invasive cytoplasmic compartment along with invading nuclear membrane.

Figure 4. *Continued*

(J) A C19MC-directed MND pathway translated and validated based on TCGA C19MC^{High} pan-cancer transcriptome. A rDNA ribosome biogenesis pathway that includes IAV+HIV infection gene signatures hold the control over NiC and its materials (cargos). Bacterial SpCas9 suppress this effect while CpG86-repeat deletion unleashes C19MC miRNAs to super-regulate the NiC. Autophagy further divides the NiC positive nuclei to generate daughter nuclei by promoting NCF from cytoplasmic side. Aurora-B functional status further determines the cytokinesis to generate daughter cells but is hampered by meiotic bridged-chromosomes to generate meiotic-bridged mini nuclei (syncytium). Daughter cells engulf other daughter cells to bring target cell nuclear DNA into cytoplasmic vacuoles where mitochondria can fuse with nDNA to generate embryonic nuclear division that can be visualized with CSi000A but not with Hoechst-33342. DDR, DNA damage repair/response pathway; NiCB, nucle(ol)ar invasive cytoplasmic bridge; NCoM, nuclear coverage of mitochondria. The ribosomes depicted are mitochondrial ribosomes, as RPS6 could be from individual proteins or from ribosomes of various cyto-locations.

Autophagy regulates NiC and MND

SpCas9 was differentially ubiquitinated between SpCas9 control and CRISPR-choppers cells (Figures 3B and 3C) and the fate of ubiquitinated protein is primarily decided by proteasomes and alternatively by autophagy. Starvation-induced autophagy doubled the number of NiC positive cells compared to fed controls upon Aurora-B inhibition, while lagging in DNA synthesis and nuclear size (Figure 4A). Furthermore, under fed conditions, inhibition of autophagy also doubled the NiC positivity (Figure 4B). Overexpression of an autophagy flux indicator (pMRX-IP-GFP-LC3-RFP)[32] in WM793 cells revealed that GFP-LC3 accumulates at perinuclear cytoplasm (Figure S4A) in baseline levels, but upon Aurora-B inhibition, autophagic degradation of GFP-LC3 occurred in the cytoplasm but not inside the NiC (Figure 4C). Autophagy is required for NCF ingression from the cytoplasmic side toward the NiC, as inhibition of autophagy resulted in the accumulation of nuclei with NiC but without NCF at the expense of cells with NCF/MND + NiC (Figure 4D). Interestingly, inhibiting CDK1 promoted DNA synthesis to a level of triploid content while suppressing NiC generation (Figure 4E). Consistently, in CRISPR-choppers cells ploidy-level DNA accumulation is prevented due to nuclear division (Figure 4F). Therefore, autophagy plays a part in generating NiC and MND by promoting the progression of NCF ingression and stalling DNA synthesis.

Inhibition of autophagy or CDK1 results in nuclear coverage of mitochondria

Next, we sought to examine the mechanism of mitochondria influx into the NiC. We hypothesized that the mitochondria are attached to the nuclear membrane and are passively drawn into the nucle(ol)ar invasive cytoplasmic compartment along with the nuclear membrane and that the mitochondria drawn inside NiC could passively bring ribosomes located within mitochondria (Figure S4B). First, CRISPR-engineered WM793 cells revealed that the total mitochondria content is regulated by C19MC, as SpCas9 suppressed mitochondrial load per cell compared to parental cells and was restored in CRISPR-choppers cells (Figure 4G). We noted a perinuclear distribution of mitochondria in SpCas9 control cells where C19MC is suppressed, but the parental and choppers cells that express C19MC exhibited a characteristic nuclear coverage of mitochondria (NCoM) (Figure 4H). Autophagy or CDK1 inhibitions in SpCas9 cells restored NCoM and improved the mitochondrial load per cell (Figures 4H and 4I). Consistently, in MCF-7 cells Aurora-B inhibition resulted in NCoM well-aligned with nuclear membrane margination of DNA during MND (Figure S4C), suggesting heterochromatinization.[22] Therefore, NCoM by C19MC determined the passive influx of mitochondria into the nucle(ol)ar invasive cytoplasmic compartment along with nuclear membrane in a CDK1 and autophagy-dependent manner (Figures 3H, 4H, and 4I). A ring-type distribution of mitochondria at the luminal periphery of NiC (Figure 2E) supports this conclusion.

NiC and MND in C19MC^{High} cancers

Finally, we examined TCGA H&E histology slides of C19MC^{High} tumors from at least 10 different cancer types to show that both NiC and MND are readily detected. NiC exhibited larger (compared to neighboring nucleoli) hematoxylin and eosin positive spot within nuclei (Figures S4D and S4E). MND on the other hand, had clear dumb-bell shaped or with multi-segmented nuclei (Figures S4D and S4E). MND can also progress in multiple planes as multi-segmented nuclei *in vitro* and result in the mixing up of cytoplasm and NiC cargoes such as RPS6 (Figure S4F). Therefore, NiC and MND are physiologically happening in C19MC^{High} clinical tumor specimens, and can be detected and distinguished from mitotic cell division on histology slides (Figure S4D versus Figure S4E).

DISCUSSION

Using TCGA pan-cancer differential gene expression profiling of C19MC^{High} tumors against C19MC^{Low} tumors, we discovered a biologically, chemically, and genetically validated mechanism for C19MC-driven MND in C19MC^{High} cancer cells (Figure 4J) and in multiple C19MC^{High} cancer subsets (Figures S4D and S1B). The genomic content is duplicated before MND, as inhibiting nucle(ol)ar invasion of cytoplasm (a step required for MND) using a CDK1 inhibitor resulted in the accumulation of triploid to tetraploid level DNA content (Figure 4E). Conversely, enabling C19MC expression by CRISPR engineering significantly reduced the number of cells accumulated with diploid genome or more DNA content (Figure 4F). Furthermore, in the MCF-7 C19MC miRNA overexpressed system, miR-519D overexpressed cell "individual nuclei" exhibited haploid DNA content upon MND compared to the control pMir overexpressed cells (Figure S1O). Despite haploid nuclei are generated, the daughter cells retained a near diploid content by a special meiosis-III type cytokinesis resulting in the packing two nuclei per daughter cell (Figures 1D and S1C). We coined the term "meiosis-III" for this type of cell division because it exhibits meiotic nuclear reduction division (meiosis-I) and gametogenic cytokinesis (meiosis-II) simultaneously (meiosis-I+II = III) instead of sequentially, and to distinguish this

type of division from regular gametogenic meiosis (Figure 1D). Considering this unique feature, it is tempting to speculate that meiosis-III could be the origin of twin embryo development in humans.

Unlike in mitosis where the mitotic spindle checkpoint ensures proper chromosome segregation between daughter cells, progression of MND of meiosis-III depends on a relatively chromosome free NCF to avoid the NoCut checkpoint. This is evident by the accumulation of MBC tangles at the nuclear cleavage furrows of miR-519D overexpressed MCF-7 cells and subsequent delay in completion of MND (Figures 1E and S1L). This delay in MND is overridden by meiotic promoter ATRA as evidenced by the reduction in sickle nuclei count (Figure 1I). As the miR-519D overexpressed MCF-7 cells continue to grow as cell line, it is conceivable that the nuclear division progresses at some point after the delay, ultimately resulting in aneuploidy/sCIN. Furthermore, lagging chromosomes were observed frequently as anaphasic bridge in C19MC miRNA overexpressed cells (Figure S1L), which can further contribute to aneuploidy (Figure S1N).

At times, meiosis-III progresses in a stealth mode, where one set of dividing genomes was not stained by Hoechst-33342 but by Cy5-CSi000A (Figures 1G, 1H, and S1I) for yet unknown mechanism, but possibly by different histone packing, methylation of chromatin, heterochromatinization (due to intense Giemsa staining at NiC: Figure S2K), or DNA conformation that could hinder Hoechst-33342 binding. We coined the term "embryonic nuclear division" (END) for these types of divisions, as it is associated with poorly differentiated ESC phenotype-enriched miR-519D cells. To detect this stealthy END, the usage of both Hoechst-33342 (20 min staining at end) and Cy5-CSi000A (24-h prior treatment or transfection, as this RNA probe is cell permeable) is recommended for live imaging. As CSi000A stains mitochondria, a mitochondrial staining pattern can be expected in cells lacking END. While END and MND can happen within the same cells (Figure S1I), an entosis-related engulfment is also possible as the END always localize inside vacuolar structures. Of note, a mixing of mitochondria with nuclear genome is rarely visualized with Hoechst-33342 plus CSi000A staining (Data not shown).

As meiotic nuclear reduction division (with nuclear membrane and anchored chromosomes) is a step that can discriminate meiotic events from mitotic events (with nuclear envelope breakdown, NEBD), we focused on the MND. MND begins with the invagination of the nuclear membrane (examined with EGFP-emerin, the inner nuclear membrane marker), which engulf nucleolus (Figure 2D subpanels A and B). As we found organelles such as mitochondria (which in turn can enclose mitochondrial ribosomes), and nucleolar marker nucleolin, we coined the term "nucleolar invasive cytoplasm/NiC." Nucle(ol)ar invasion of mitochondria and other cargoes is followed by autophagic ingression of NCF to proceed with MND (Figures 4J and S4F). MND is orchestrated by IAV+HIV infection gene signatures (rDNA, ribosome biogenesis pathway) by regulating the NiC and cargo traffic.

MND is governed by Aurora-B and CDK1 kinases to regulate the efflux and influx of protein and organelle cargoes respectively to ultimately regulate NiC size and NCF-driven division through autophagy. While protein cargos can shuttle between the nucleoplasm and cytoplasm through nuclear pore complex, organelle influx must have a different mode of nucle(ol)ar entry. We found that C19MC miRNAs regulated the NCoM where the mitochondria localize to the nuclear surface (Figure 4H). Thus, a nuclear membrane invagination event could slide the mitochondria into the NiC. Organelle influx into the NiC is trafficked through the nucle(ol)ar invasive cytoplasmic bridge (NiCB) by passive sliding of nuclear membrane tethered mitochondria (NiCB: Figures 2E, 4J, S3G, and S4B). Emerin strings (eStrings) clearly showed a mechanistic role of the inner nuclear membrane in holding the sickle nuclear shape and is a good indicator of MBC directed activation of the NoCut checkpoint. The sickle nuclear phenotype also reflects the functionally defective status of ESCRT and Aurora-B. Therefore, we used sickle nuclear count as a measure of C19MC-directed MND.

Suppression of C19MC by SpCas9 raises a serious concern of SpCas9-directed CRISPR therapeutics, requiring further studies. The reversal of SpCas9-directed inhibition of C19MC expression by CRISPR-choppers that deletes CpG86 repeats demonstrated the pivotal role of CpG86 in C19MC regulation. Despite a previous study by Noguer-Dance et al.[33] had first implicated that CpG86 repeats have promoter activity by luciferase experiments; our current study is the first to demonstrate a direct cause-effect relationship of CpG86 13-repeats to C19MC expression by CRISPR engineering of the human genome. Of note, pediatric cancers (UESL and ETMR) with high C19MC expression are found to have chromosomal translocations at C19MC upstream regions. However, it is not experimentally validated that whether the translocation-assisted CpG86 displacement is the cause of C19MC hyperexpression in these pediatric cancers to date. Therefore, our study in part explains why pediatric cancers with high C19MC expression have the CpG86 relocated from C19MC landscape by chromosomal rearrangements.[13,14]

Considering the pivotal role of Aurora-B in C19MC function on MND and multinucleation, the functional status of Aurora-B could be the main determinant of restricting viruses by C19MC, as the multinucleated placental syncytiotrophoblasts but not the mononucleated cytotrophoblasts[1,2] restrict viruses to control vertical transmission of viruses.

Overall, these findings demonstrate a novel meiosis-III, MND, which is driven by C19MC-induced nucle(ol)ar invasion of protein and mitochondria cargoes, and implicate potential impacts on multiple research and therapeutic areas including cancer to pathogen interactions, immunotherapy, vertical transmission of viruses in human/primate placenta, antiviral research and SpCas9-directed CRISPR therapeutics.

Limitations of the study

Considering the fact that the C19MC miRNAs are expressed in an all-or-none fashion, the initial part of our study on individual miRNA overexpression sheds light only on the function of few miRNAs out of 46 miRNAs, especially on the role of miR-519D in delaying MND. However, when we examined the C19MC function using anti-miR-519D, these single anti-miRs can have C19MC-wide sponging effects due to the sequence similarity of the mature C19MC miRNAs. Therefore, the anti-miR-519D effect on phenotypes cannot be attributed to blocking/sponging of miR-519D alone. To circumvent this issue, we used the CRISPR-engineered and control cells to demonstrate the role of C19MC in MND where the C19MC miRNAs exhibit an on/off pattern. However, how spCas9 suppressed C19MC miRNA expression remains to be determined and its characterization is beyond the scope of this study. Furthermore, it is possible that other mechanisms may exist to

influence MND in a cell/tissue type dependent fashion. Finally, functional Aurora-B function-dependent override of MND highlights that the C19MC may not restrict viruses in every cell type in which it is expressed if Aurora-B is active.

RESOURCE AVAILABILITY

Lead contact

Further information and requests for details on materials should be directed to and will be fulfilled by the lead contact, Dr. Goodwin G. Jinesh (goodwinjinesh@gmail.com).

Materials availability

Further information and requests for materials should be directed to and will be fulfilled by the corresponding author contact, Dr. Andrew S. Brohl (Andrew.Brohl@moffitt.org).

Data and code availability

- Any additional information related to the data reported in this paper is available from the lead contact upon request.
- This paper does not report original codes but uses modified codes, which are given under appropriate sections of STAR Methods online.
- This paper uses public TCGA datasets, and details are given below under the appropriate methods sections.

ACKNOWLEDGMENTS

The results shown here are in part based upon data generated by TCGA Research Network: https://www.cancer.gov/tcga. The results published here are in part based upon data generated by The Cancer Genome Atlas managed by the NCI, NHGRI, and dbGAP. Information about TCGA can be found at http://cancergenome.nih.gov. We sincerely thank TCGA network research groups for the data; Dr. Katherine L. Wilson (JHMI, Baltimore, USA) for EGFP-EMD/emerin plasmid; Dr. Noboru Mizushima (The University of Tokyo, Tokyo Japan) for pMRX-IP-GFP-LC3-RFP (Addgene plasmid: 84573); Dr. Feng Zhang (Broad Institute of Massachusetts Institute of Technology and Harvard, Massachusetts, USA) for pSpCas9(BB)-2A-Puro (PX459) V2.0 (Addgene plasmid: 62988); Ms. Nicole Hackel, Ms. Payal Raulji, and Ms. Bethanie Gore (Moffitt Cancer Center, Tampa, FL, USA) for acquiring reagents; Drs. Keiran S.M. Smalley, Manali S. Phadke, Xiaobo Li, Avani A. Deshpande, Gina DeNicola, Brian J. Czerniecki, Wiener Doris, Kodumudi N. Krithika (Moffitt Cancer Center, Tampa, FL, USA), Lewis S. Jason, and Patricia Manuela (Memorial Sloan Kettering Cancer Center, USA) for providing cell lines; and Dr. Hayley D. Ackerman for helps in cell line authentication. Research reported in this publication was supported in part by the National Institutes of Health under award number K08CA255933. Funding for publication of this work was supported by the AmandaLee Sarcoma Fund, Moffitt Cancer Center.

AUTHOR CONTRIBUTIONS

G.G.J. conceived and identified the meiosis-III, NiC, MND, NCoM aspects, designed the study, performed experiments, data analysis, interpretation, and R and other visualizations, wrote and revised the manuscript. A.S.B. conceived the target C19MC, assisted in TCGA C19MC^{High} vs. C19MC^{Low} patient stratification and contributed to funds. Nino M. assisted with CRISPR-guide cloning. M.T.S. performed shRNA knock-down attempts (data not included). Marco N. performed regular quality control of all cell lines. J.H.L. attempted to develop an app to quantify NCoM (App not included) and assisted with bioinformatics. A.S.B., E.R.F., J.H.L., and M.N. edited the manuscript. A.S.B. and E.R.F. supervised the study. All authors read and agree to the entire contents of the manuscript.

DECLARATION OF INTERESTS

The authors G.G.J. and A.S.B. have a provisional patent application pending for the RNA probe Cy5-CSi000A and CRISPR-CpG86-chopper guides-1 and 2. A.S.B. has advisory board relationships with Bayer and Deciphera.

STAR★METHODS

Detailed methods are provided in the online version of this paper and include the following:

- KEY RESOURCES TABLE
- EXPERIMENTAL MODEL AND STUDY PARTICIPANT DETAILS
  - Human subject statement
  - IBC approval
  - Cell lines, and constructs
- METHOD DETAILS
  - Pan-cancer clinical datasets and data processing
  - C19MC^{High} versus C19MC^{Low} gene set enrichment analyses (GSEAs) and visualizations in R
  - CCLE 954 cell line cumulative C19MC expression analysis
  - CCLE 1020 cell line IAV, HIV, and shared signature analysis
  - dbGAP data access and IGV visualization of C19MC transcriptional landscape
  - EnrichR analyses
  - Bird's eye view volcano plot: Meiotic-regulatory gene expression in C19MC^{High} groups of TGCT vs. THYM
  - Cell lines: Authentication, quality control and maintenance
  - Chemical reagents/inhibitors and usage
  - Protein hormone, enzymes, kits, antibodies, transfection reagents and usage
  - Genetic reagents (anti-miRNAs, RNA-probes)
  - Genetic reagents (plasmid DNAs) and stable cell lines generated: No viruses
  - CRISPR guide RNA cloning and Sanger sequencing
  - CRISPR genetic engineering of CpG86
  - Sanger sequencing of CRISPRed genomic regions
  - CpG86: 13-repeat hypervariability test
  - Genomic DNA CRISPR screening PCRs, colony PCRs and primers
  - Transient gene/anti-miR transfections

- Stable transfections of single C19MC miRNAs and cell sorting
- Microscopy
- Nucle(ol)ar invasion of cytoplasm [NiC] assays
- Detection of mitochondria within nucle(ol)ar invasive cytoplasm
- Detecting Giemsa positive DNA, and mitochondria within the closed nucle(ol)ar invasive cytoplasm
- Quantification of mitochondria traffic into the nucle(ol)ar invasive cytoplasmic compartment and visualization in R
- Immunofluorescence
- Quantification of nucleolin, RPS6, REST/NRSF traffic into the nucle(ol)ar invasive cytoplasmic compartment and visualization in R
- Detection of autophagic flux within sub-cellular locations [Cytoplasmic vs. nucle(ol)ar invasive cytoplasm]
- Starvation-induced autophagy, autophagy inhibition experiments, and data visualization in R
- Western immunoblotting
- Tracking proteasomal degradation of SpCas9
- Cytogenetics: structural chromosomal instability
- Cytogenetics: numerical chromosomal instability (nCIN)
- Meiotic nuclear division imaging of isolated nuclei
- Evaluation of DNA content reduction during meiotic nuclear division among daughter nuclei
- Nocodazole/Colchicine arrest and release of Meiosis-III cells
- Well-differentiated vs. Poorly-differentiated colony counts
- Nuclear counts in living cells
- Embryonic nuclear division (END) visualization in living cells
- Metal response stimulation of endogenous C19MC miRs
- Quantitative real-time-PCRs (qRT-PCRs) and reverse transcriptase PCRs (RT-PCRs)
- Nuclear coverage of mitochondria (NCoM) quantification and visualization in R
- TCGA H&E diagnostic slides/histology
- Nuclear margination of chromatin and mitochondria in living cells
- Softwares, packages, web-servers used and figure compositing

- QUANTIFICATION AND STATISTICAL ANALYSES

SUPPLEMENTAL INFORMATION

Supplemental information can be found online at https://doi.org/10.1016/j.isci.2024.111132.

Received: January 23, 2024
Revised: June 26, 2024
Accepted: October 7, 2024
Published: October 10, 2024

REFERENCES

1. Delorme-Axford, E., Sadovsky, Y., and Coyne, C.B. (2014). The Placenta as a Barrier to Viral Infections. Annu. Rev. Virol. *1*, 133–146. https://doi.org/10.1146/annurev-virology-031413-085524.
2. Delorme-Axford, E., Donker, R.B., Mouillet, J.-F., Chu, T., Bayer, A., Ouyang, Y., Wang, T., Stolz, D.B., Sarkar, S.N., Morelli, A.E., et al. (2013). Human placental trophoblasts confer viral resistance to recipient cells. Proc. Natl. Acad. Sci. USA *110*, 12048–12053. https://doi.org/10.1073/pnas.1304718110.
3. Jinesh, G.G., Smallin, M.T., Mtchedlidze, N., Godwin, I., Napoli, M., Hackel, N., Phadke, M.S., Deshpande, A.A., Li, X., Lockhart, J.H., et al. (2024). C19MC miRNA-520G induces *SP100* antiviral gene transcription and inhibits melanin production in skin cutaneous melanoma. Genes Dis. *11*, 60–63. https://doi.org/10.1016/j.gendis.2023.02.047.
4. Jinesh, G.G., and Brohl, A.S. (2020). The genetic script of metastasis. Biol. Rev. Camb. Philos. Soc. *95*, 244–266. https://doi.org/10.1111/brv.12562.
5. Bortolin-Cavaillé, M.L., Dance, M., Weber, M., and Cavaillé, J. (2009). C19MC microRNAs are processed from introns of large Pol-II, non-protein-coding transcripts. Nucleic Acids Res. *37*, 3464–3473. https://doi.org/10.1093/nar/gkp205.
6. Jinesh, G.G., and Kamat, A.M. (2017). The Blebbishield Emergency Program Overrides Chromosomal Instability and Phagocytosis Checkpoints in Cancer Stem Cells. Cancer Res. *77*, 6144–6156. https://doi.org/10.1158/0008-5472.CAN-17-0522.
7. Fujiwara, T., Bandi, M., Nitta, M., Ivanova, E.V., Bronson, R.T., and Pellman, D. (2005). Cytokinesis failure generating tetraploids promotes tumorigenesis in p53-null cells. Nature *437*, 1043–1047. https://doi.org/10.1038/nature04217.
8. Holland, A.J., and Cleveland, D.W. (2009). Boveri revisited: chromosomal instability, aneuploidy and tumorigenesis. Nat. Rev. Mol. Cell Biol. *10*, 478–487. https://doi.org/10.1038/nrm2718.
9. Jinesh, G.G., and Brohl, A.S. (2022). Classical epithelial-mesenchymal transition (EMT) and alternative cell death process-driven blebbishield metastatic-witch (BMW) pathways to cancer metastasis. Signal Transduct. Target. Ther. *7*, 296. https://doi.org/10.1038/s41392-022-01132-6.
10. Jinesh, G.G., and Kamat, A.M. (2016). Endocytosis and serpentine filopodia drive blebbishield-mediated resurrection of apoptotic cancer stem cells. Cell Death Discov. *2*, 15069. https://doi.org/10.1038/cddiscovery.2015.69.
11. Jinesh, G.G., Sambandam, V., Vijayaraghavan, S., Balaji, K., and Mukherjee, S. (2018). Molecular genetics and cellular events of K-Ras-driven tumorigenesis. Oncogene *37*, 839–846. https://doi.org/10.1038/onc.2017.377.
12. Godwin, I., Anto, N.P., Bava, S.V., Babu, M.S., and Jinesh, G.G. (2021). Targeting K-Ras and apoptosis-driven cellular transformation in cancer. Cell Death Discov. *7*, 80. https://doi.org/10.1038/s41420-021-00457-5.
13. Setty, B.A., Jinesh, G.G., Arnold, M., Pettersson, F., Cheng, C.H., Cen, L., Yoder, S.J., Teer, J.K., Flores, E.R., Reed, D.R., and Brohl, A.S. (2020). The genomic landscape of undifferentiated embryonal sarcoma of the liver is typified by C19MC structural rearrangement and overexpression combined with TP53 mutation or loss. PLoS Genet. *16*, e1008642. https://doi.org/10.1371/journal.pgen.1008642.
14. Archer, T.C., and Pomeroy, S.L. (2014). A developmental program drives aggressive embryonal brain tumors. Nat. Genet. *46*, 2–3. https://doi.org/10.1038/ng.2857.
15. Jinesh, G.G., Flores, E.R., and Brohl, A.S. (2018). Chromosome 19 miRNA cluster and CEBPB expression specifically mark and potentially drive triple negative breast cancers. PLoS One *13*, e0206008. https://doi.org/10.1371/journal.pone.0206008.
16. Jinesh, G.G., Napoli, M., Ackerman, H.D., Raulji, P.M., Montey, N., Flores, E.R., and Brohl, A.S. (2020). Regulation of MYO18B mRNA by a network of C19MC miRNA-520G, IFN-gamma, CEBPB, p53 and bFGF in hepatocellular carcinoma. Sci. Rep. *10*, 12371. https://doi.org/10.1038/s41598-020-69179-5.
17. Jinesh, G.G., Napoli, M., Smallin, M.T., Davis, A., Ackerman, H.D., Raulji, P., Montey, N., Flores, E.R., and Brohl, A.S. (2021). Mutant p53s and chromosome 19 microRNA cluster overexpression regulate cancer testis antigen expression and cellular transformation in hepatocellular carcinoma. Sci. Rep. *11*, 12673. https://doi.org/10.1038/s41598-021-91924-7.

18. Pellegrini, M., Filipponi, D., Gori, M., Barrios, F., Lolicato, F., Grimaldi, P., Rossi, P., Jannini, E.A., Geremia, R., and Dolci, S. (2008). ATRA and KL promote differentiation toward the meiotic program of male germ cells. Cell Cycle *7*, 3878–3888. https://doi.org/10.4161/cc.7.24.7262.
19. Amaral, N., Vendrell, A., Funaya, C., Idrissi, F.-Z., Maier, M., Kumar, A., Neurohr, G., Colomina, N., Torres-Rosell, J., Geli, M.-I., and Mendoza, M. (2016). The Aurora-B-dependent NoCut checkpoint prevents damage of anaphase bridges after DNA replication stress. Nat. Cell Biol. *18*, 516–526. https://doi.org/10.1038/ncb3343.
20. Carlton, J.G., Caballe, A., Agromayor, M., Kloc, M., and Martin-Serrano, J. (2012). ESCRT-III Governs the Aurora B–Mediated Abscission Checkpoint Through CHMP4C. Science *336*, 220–225. https://doi.org/10.1126/science.1217180.
21. Lee, K.K., Haraguchi, T., Lee, R.S., Koujin, T., Hiraoka, Y., and Wilson, K.L. (2001). Distinct functional domains in emerin bind lamin A and DNA-bridging protein BAF. J. Cell Sci. *114*, 4567–4573. https://doi.org/10.1242/jcs.114.24.4567.
22. Ungricht, R., and Kutay, U. (2017). Mechanisms and functions of nuclear envelope remodelling. Nat. Rev. Mol. Cell Biol. *18*, 229–245. https://doi.org/10.1038/nrm.2016.153.
23. Wang, L., Li, L., Wu, X., Wong, C.K.C., Perrotta, A., Silvestrini, B., Sun, F., and Cheng, C.Y. (2022). mTORC1/rpS6 and p-FAK-Y407 signaling regulate spermatogenesis: Insights from studies of the adjudin pharmaceutical/toxicant model. Semin. Cell Dev. Biol. *121*, 53–62. https://doi.org/10.1016/j.semcdb.2021.03.024.
24. Hirose, T., Ninomiya, K., Nakagawa, S., and Yamazaki, T. (2023). A guide to membraneless organelles and their various roles in gene regulation. Nat. Rev. Mol. Cell Biol. *24*, 288–304. https://doi.org/10.1038/s41580-022-00558-8.
25. Hori, Y., Engel, C., and Kobayashi, T. (2023). Regulation of ribosomal RNA gene copy number, transcription and nucleolus organization in eukaryotes. Nat. Rev. Mol. Cell Biol. *24*, 414–429. https://doi.org/10.1038/s41580-022-00573-9.
26. Hiscox, J.A. (2002). The nucleolus–a gateway to viral infection? Arch. Virol. *147*, 1077–1089. https://doi.org/10.1007/s00705-001-0792-0.
27. Tiwari, M., and Chaube, S.K. (2017). Maturation promoting factor destabilization mediates human chorionic gonadotropin induced meiotic resumption in rat oocytes. Dev. Growth Differ. *59*, 603–614. https://doi.org/10.1111/dgd.12387.
28. Li, H., and Clagett-Dame, M. (2009). Vitamin A deficiency blocks the initiation of meiosis of germ cells in the developing rat ovary in vivo. Biol. Reprod. *81*, 996–1001. https://doi.org/10.1095/biolreprod.109.078808.
29. Ran, F.A., Hsu, P.D., Wright, J., Agarwala, V., Scott, D.A., and Zhang, F. (2013). Genome engineering using the CRISPR-Cas9 system. Nat. Protoc. *8*, 2281–2308. https://doi.org/10.1038/nprot.2013.143.
30. Ergünay, T., Ayhan, Ö., Celen, A.B., Georgiadou, P., Pekbilir, E., Abaci, Y.T., Yesildag, D., Rettel, M., Sobhiafshar, U., and Ogmen, A. (2022). Sumoylation of Cas9 at lysine 848 regulates protein stability and DNA binding. Life Sci. Alliance *5*, e202101078.
31. Li, Z., Chen, S., Zhao, L., Huang, G., Xu, H., Yang, X., Wang, P., Gao, N., and Sui, S.-F. (2023). Nuclear export of pre-60S particles through the nuclear pore complex. Nature *618*, 411–418. https://doi.org/10.1038/s41586-023-06128-y.
32. Kaizuka, T., Morishita, H., Hama, Y., Tsukamoto, S., Matsui, T., Toyota, Y., Kodama, A., Ishihara, T., Mizushima, T., and Mizushima, N. (2016). An Autophagic Flux Probe that Releases an Internal Control. Mol. Cell *64*, 835–849. https://doi.org/10.1016/j.molcel.2016.09.037.
33. Noguer-Dance, M., Abu-Amero, S., Al-Khtib, M., Lefèvre, A., Coullin, P., Moore, G.E., and Cavaillé, J. (2010). The primate-specific microRNA gene cluster (C19MC) is imprinted in the placenta. Hum. Mol. Genet. *19*, 3566–3582. https://doi.org/10.1093/hmg/ddq272.
34. Wickham, H. (2009). ggplot2: Elegant Graphics for Data Analysis (Springer), pp. 1–213. https://doi.org/10.1007/978-0-387-98141-3.
35. Robinson, J.T., Thorvaldsdóttir, H., Winckler, W., Guttman, M., Lander, E.S., Getz, G., and Mesirov, J.P. (2011). Integrative genomics viewer. Nat. Biotechnol. *29*, 24–26. https://doi.org/10.1038/nbt.1754.
36. Kuleshov, M.V., Jones, M.R., Rouillard, A.D., Fernandez, N.F., Duan, Q., Wang, Z., Koplev, S., Jenkins, S.L., Jagodnik, K.M., Lachmann, A., et al. (2016). Enrichr: a comprehensive gene set enrichment analysis web server 2016 update. Nucleic Acids Res. *44*, W90–W97. https://doi.org/10.1093/nar/gkw377.
37. Chen, E.Y., Tan, C.M., Kou, Y., Duan, Q., Wang, Z., Meirelles, G.V., Clark, N.R., and Ma'ayan, A. (2013). Enrichr: interactive and collaborative HTML5 gene list enrichment analysis tool. BMC Bioinf. *14*, 128. https://doi.org/10.1186/1471-2105-14-128.
38. Xie, Z., Bailey, A., Kuleshov, M.V., Clarke, D.J.B., Evangelista, J.E., Jenkins, S.L., Lachmann, A., Wojciechowicz, M.L., Kropiwnicki, E., Jagodnik, K.M., et al. (2021). Gene Set Knowledge Discovery with Enrichr. Curr. Protoc. *1*, e90. https://doi.org/10.1002/cpz1.90.
39. Prasad, S., Koch, B., and Chaube, S.K. (2016). Maturation promoting factor destabilization facilitates postovulatory aging-mediated abortive spontaneous egg activation in rat. Dev. Growth Differ. *58*, 293–302. https://doi.org/10.1111/dgd.12272.
40. Jinesh, G.G., Molina, J.R., Huang, L., Laing, N.M., Mills, G.B., Bar-Eli, M., and Kamat, A.M. (2016). Mitochondrial oligomers boost glycolysis in cancer stem cells to facilitate blebbishield-mediated transformation after apoptosis. Cell Death Discov. *2*, 16003. https://doi.org/10.1038/cddiscovery.2016.3.
41. Jinesh, G.G., Laing, N.M., and Kamat, A.M. (2016). Smac mimetic with TNF-alpha targets Pim-1 isoforms and reactive oxygen species production to abrogate transformation from blebbishields. Biochem. J. *473*, 99–107. https://doi.org/10.1042/BJ20150877.
42. Claus, O.W. (2022). ggridges: Ridgeline Plots in 'ggplot2'. R package version 0.5.4. ggRidges.
43. Jinesh, G.G., and Kamat, A.M. (2017). RalBP1 and p19-VHL play an oncogenic role, and p30-VHL plays a tumor suppressor role during the blebbishield emergency program. Cell Death Discov. *3*, 17023. https://doi.org/10.1038/cddiscovery.2017.23.
44. Fletcher, J. (2001). Metaphase harvest and cytogenetic analysis of solid tumor cultures. Curr. Protoc. Hum. Genet. *Chapter 10*. Unit 10.3. https://doi.org/10.1002/0471142905.hg1003s02.
45. Jinesh, G.G., Choi, W., Shah, J.B., Lee, E.K., Willis, D.L., and Kamat, A.M. (2013). Blebbishields, the emergency program for cancer stem cells: sphere formation and tumorigenesis after apoptosis. Cell Death Differ. *20*, 382–395. https://doi.org/10.1038/cdd.2012.140.

STAR★METHODS

KEY RESOURCES TABLE

REAGENT or RESOURCE	SOURCE	IDENTIFIER
Antibodies		
Rabbit anti-SYCP2 antibody [Usage: 1:250 (Immunofluorescence)]	Sigma	RRID: AB_2684752; Cat# HPA062401
REST/NRSF antibody [Usage: 1:100 (Immunofluorescence); 1:500 (Western blotting)]	Santacruz Biotechnology	RRID: AB_10988033; Cat# sc-374611
Nucleolin/C23 antibody [Usage: 1:100 (Immunofluorescence)]	Santacruz Biotechnology	RRID: AB_670270; Cat# sc-17826
RPS6 antibody [Usage: 1:100 (Immunofluorescence)]	Santacruz Biotechnology	RRID: AB_1129205; Cat# sc-74459
β-Tubulin antibody [Usage: 1:100 (Immunofluorescence)]	Santacruz Biotechnology	RRID: AB_2010699; Cat# Sc-166729
SpCas9 antibody [Clone: 14B6] [Usage: 1:250 (Immunofluorescence); 1:500 (Western blotting); Dilutions from 5 μg/ml stock.]	Genscript/ThermoFisher	RRID: NA; Cat# A01936-40
Goat anti-Mouse IgG (H+L) Cross-Adsorbed Secondary Antibody, Cyanine5 [Usage: 1:1000 (Immunofluorescence)]	Life Technologies	RRID: AB_10562712; Cat# A10524
Goat anti-Rabbit IgG (H+L) Cross-Adsorbed Secondary Antibody, Cyanine5 [Usage: 1:1000 (Immunofluorescence)]	Life Technologies	RRID: AB_1500679; Cat# A10523
F(ab)2-Goat anti-Rabbit IgG (H+L) Cross-Adsorbed Secondary Antibody, Alexa Fluor 555 [Usage: 1:1000 (Immunofluorescence)]	Life Technologies	RRID: AB_2535851; Cat# A-21430
Li-COR Goat anti-mouse secondary antibody-680LT [Western blotting usage: 1:5000]	Li-COR	RRID: NA; Cat#925-88020
Li-COR Goat anti-rabbit secondary antibody-800CW [Western blotting usage: 1:5000]	Li-COR	RRID: NA; Cat#926-32211
Bacterial and viral strains		
pSpCas9(BB)-2A-Puro (PX459) V2.0 [No added Guide-sgRNA cassette [NG: Has in-built non-targeting sequence between BbsI sites]; Stable in WM793 as pooled cells [NGP]	Addgene	62988
pSpCas9(BB)-2A-Puro (PX459) V2.0-Chopper-1 [5′-GGGCACGGTGGTTCCCATCA-3′-sgRNA-guide sequence]; Stable in WM793 as pooled cells [Choppers-P]	Cloned (See STAR methods for cloning and transfection procedures; Choppers-1 and 2 were transfected together)	NA
pSpCas9(BB)-2A-Puro (PX459) V2.0-Chopper-2 [5′- AGAGGGGTCCAGGCTGGGCA-3′-sgRNA-guide sequence]; Stable in WM793 as pooled cells [Choppers-P]	Cloned (See STAR methods for cloning and transfection procedures; Choppers-1 and 2 were transfected together)	NA
Subcloning Efficiency DH5α Competent Cells [Usage: Manufacturer's recommendations]	Life Technologies	RRID: NA; Cat#18265017
Chemicals, peptides and recombinant proteins		
All-trans-retinoic acid (ATRA) [Dose used: 1 μM]	Cayman Chemicals	11017
Hoechst-33342 [Dose used: 10 nM]	Cayman Chemicals	15547
Aurora-B inhibitor AZD1152-HQPA [Dose used: 20 nM]	Cayman Chemicals	11602

(*Continued on next page*)

Continued

REAGENT or RESOURCE	SOURCE	IDENTIFIER
Actinomycin-D [Dose used: 1 ng/ml & 10 ng/ml(Dose selected to inhibit NiC formation)]	Cayman Chemicals	11421
JC-1 mitochondria labeling agent [Dose used: 1 μg/ml]	Cayman Chemicals	15003
CDK1 inhibitor Ro 3306 [Dose used: 10 μM]	Cayman Chemicals	15149-5
(S)-MG132 [Dose used: 0.1 μM & 1 μM (Dose selected to inhibit NiC formation)]	Cayman Chemicals	10012628-5
Leptomycin-B (LMB) [Dose used: 10 ng/ml(Dose selected to inhibit NiC formation)]	Cayman Chemicals	10004976-10
Chloroquine (CQ) [Dose used: 20 μM]	Cayman Chemicals	14194
Cycloheximide (CHX) [Dose used: 10 μg/ml]	Sigma	01810
Zinc chloride [Dose used: 200 μM – 1 mM]	Sigma	208086
Wright's modified Giemsa [Conc. used: 2%]	Sigma	WG16
Nocodazole [Dose used: 400 ng/ml]	Sigma	M1404
Colcemid [Dose used: 20 ng/ml]	Sigma	15364
DMSO [Dose used: 1 μl/ml; 2 μl/ml (Serves as control if combination of two DMSO dissolved agents involved)]	Sigma	D8418
190 proof ethyl alcohol [Dose used: 1 μl/ml]	Pharmco-Greenfield Global	111000190
Methanol [Dose used: 1 μl/ml]	Fisher Scientific	A4524
5M betaine [Dose used: 1M final.]	Sigma	B0300-1VL
Human chorionic gonadotrophin polypeptides A and B [hCG] [Usage: 25 ng/ml]	R&D Systems	RRID: NA; Cat#7727-CG-010/CF
Fast Digest BbsI restriction enzyme [Usage: Manufacturer's recommendation]	New England Biolabs	RRID: NA; Cat# R3539S
SOC media [Usage: Manufacturer's recommendation]	G-Biosciences	RRID: NA; Cat#786-1280
Opti-MEM [Usage: Manufacturer's recommendation]	Gibco	RRID: NA; Cat#31985070
Critical commercial assays		
Lipofectamine 2000 [Usage: Manufacturer's recommendation]	Life Technologies	RRID: NA; Cat#11668019
Lipofectamine RNAiMAX [Usage: Manufacturer's recommendation]	Invitrogen	RRID: NA; Cat#13778075
LigaFast Rapid DNA Ligation System [Usage: Manufacturer's recommendation]	Promega	RRID: NA; Cat# M8221
Plasmid MIDI-prep kit [Usage: Manufacturer's recommendation]	Qiagen	RRID: NA; Cat#12143
Plasmid Mini-prep kit [Usage: Manufacturer's recommendation]	Qiagen	RRID: NA; Cat#27104
Illustra GFX PCR DNA and Gel Band Purification Kit [Usage: Manufacturer's recommendation]	GE Healthcare	RRID: NA; Cat#28903470
QIAamp DNA mini kit [Usage: Manufacturer's recommendation]	Qiagen	RRID: NA; Cat#51304
pGEM-T Easy -TA cloning kit [Usage: Manufacturer's recommendation]	Promega	RRID: NA; Cat# A1360
miRNeasy Mini Kit [Usage: Manufacturer's recommendation]	Qiagen	RRID: NA; Cat#217004
TaqMan MicroRNA Reverse Transcription Kit [Usage: Manufacturer's recommendation]	ThermoFisher/ABI	RRID: NA; Cat#4366596

(*Continued on next page*)

Continued

REAGENT or RESOURCE	SOURCE	IDENTIFIER
Trizol [Usage: Manufacturer's recommendation]	ThermoFisher Scientific	RRID: NA; Cat#15596026
GeneRuler 100 bp DNA Ladder [Usage: 2.5 µl/ lane]	ThermoFisher Scientific	RRID: NA; Cat# SM0243
RNU6B Control (For qRT-PCR)	ThermoFisher	Assay ID: 001093 ; Cat# 4427975
hsa-miR-519d-3p (For qRT-PCR)	ThermoFisher	Assay ID: 002403 ; Cat# 4427975
hsa-miR-520g-3p (For qRT-PCR)	ThermoFisher	Assay ID: 001121 ; Cat# 4427975
hsa-miR-526b-3p (For qRT-PCR)	ThermoFisher	Assay ID: 002383 ; Cat# 4427975
TaqMan Universal PCR Master Mix (For qRT-PCR)	Life Technologies	Assay ID: NA ; Cat# 4324018
High-Capacity cDNA Reverse Transcription Kit (cDNA synthesis for (q)RT-PCR.	ABI	Cat# 4368814
Experimental models: Cell lines		
MCF-7 [Breast, MEM with 10% FBS + Nonessential amino acids, Penstrep, L-Glutamine, Sodium Pyruvate, & Vitamins, STR-Confirmed, Mycoplasma negative]	Local: Drs. Elsa R. Flores & Xiaobo Li, Moffitt Cancer Center, FL, USA; Commercial: ATCC, Cat# HTB22	RRID: CVCL_0031
T47D [Breast, MEM with 10% FBS + Nonessential amino acids, Penstrep, L-Glutamine, Sodium Pyruvate, & Vitamins, STR-Confirmed, Mycoplasma negative]	Local: Drs. Brian J. Czerniecki, Wiener Doris, Kodumudi N. Krithika, Moffitt Cancer Center, Tampa, FL, USA; Commercial: ATCC, Cat# HTB-133	RRID: CVCL_0553
BT-459 [Breast, MEM with 10% FBS + Nonessential amino acids, Penstrep, L-Glutamine, Sodium Pyruvate, & Vitamins, STR-Confirmed, Mycoplasma negative]	Local: Drs. Brian J. Czerniecki, Wiener Doris, Kodumudi N. Krithika, Moffitt Cancer Center, Tampa, FL, USA; Commercial: ATCC, Cat# HTB-122	RRID: CVCL_1092
MDA-MB-157 [Breast, MEM with 10% FBS + Nonessential amino acids, Penstrep, L-Glutamine, Sodium Pyruvate, & Vitamins, STR-Confirmed, Mycoplasma negative]	Local: Drs. Brian J. Czerniecki, Wiener Doris, Kodumudi N. Krithika, Moffitt Cancer Center, Tampa, FL, USA; Commercial: ATCC, Cat# HTB-24	RRID: CVCL_0618
MDA-MB-231 [Breast, MEM with 10% FBS + Nonessential amino acids, Penstrep, L-Glutamine, Sodium Pyruvate, & Vitamins, STR-Confirmed, Mycoplasma negative]	Local: Drs. Brian J. Czerniecki, Wiener Doris, Kodumudi N. Krithika, Moffitt Cancer Center, Tampa, FL, USA; Commercial: ATCC, Cat# HTB-26	RRID: CVCL_0062
MDA-MB-436 [Breast, MEM with 10% FBS + Nonessential amino acids, Penstrep, L-Glutamine, Sodium Pyruvate, & Vitamins, STR-Confirmed, Mycoplasma negative]	Local: Drs. Brian J. Czerniecki, Wiener Doris, Kodumudi N. Krithika, Moffitt Cancer Center, Tampa, FL, USA; Commercial: ATCC, Cat# HTB-130	RRID: CVCL_0623
MDA-MB-468 [Breast, MEM with 10% FBS + Nonessential amino acids, Penstrep, L-Glutamine, Sodium Pyruvate, & Vitamins, STR-Confirmed, Mycoplasma negative]	Local: Drs. Brian J. Czerniecki, Wiener Doris, Kodumudi N. Krithika, Moffitt Cancer Center, Tampa, FL, USA; Commercial: ATCC, Cat# HTB-132	RRID: CVCL_0419
HepG2 [Liver, MEM with 10% FBS + Nonessential amino acids, Penstrep, L-Glutamine, Sodium Pyruvate, & Vitamins, STR-Confirmed, Mycoplasma negative]	Local: Dr. Gina DeNicola, Moffitt Cancer Center, FL, USA; Commercial: ATCC, Cat# HB-8065	RRID: CVCL_0027
Hep3B [Liver, MEM with 10% FBS + Nonessential amino acids, Penstrep, L-Glutamine, Sodium Pyruvate, & Vitamins, STR-Confirmed, Mycoplasma negative]	Local: Dr. Andrew S. Brohl, Moffitt Cancer Center, FL, USA; Commercial: ATCC, Cat# HB-8064	RRID: CVCL_0326
SKHep1 [Liver, MEM with 10% FBS + Nonessential amino acids, Penstrep, L-Glutamine, Sodium Pyruvate, & Vitamins, STR-Confirmed, Mycoplasma negative]	Local: Dr. Andrew S. Brohl, Moffitt Cancer Center, FL, USA; Commercial: ATCC, Cat# HTB-52	RRID: CVCL_0525

(*Continued on next page*)

Continued

REAGENT or RESOURCE	SOURCE	IDENTIFIER
HLF [Liver, MEM with 10% FBS + Nonessential amino acids, Penstrep, L-Glutamine, Sodium Pyruvate, & Vitamins, STR-Confirmed, Mycoplasma negative]	Local: Dr. Andrew S. Brohl, Moffitt Cancer Center, FL, USA; Commercial: JCRB: Cat# JCRB0405	RRID: CVCL_2947
SNU-182 [Liver, RPMI with HEPES, 10% FBS + Nonessential amino acids, Penstrep, L-Glutamine, Sodium Pyruvate, & Vitamins, STR-Confirmed, Mycoplasma negative]	Local: Dr. Andrew S. Brohl, Moffitt Cancer Center, FL, USA; Commercial: ATCC: Cat# CRL-2235	RRID: CVCL_0090
HEK293T [Kidney, MEM with 10% FBS + Nonessential amino acids, Penstrep, L-Glutamine, Sodium Pyruvate, & Vitamins, STR-Confirmed, Mycoplasma negative]	Local: Dr. Elsa R. Flores & Ms. Avani Deshpande, Moffitt Cancer Center, FL, USA; Commercial: ATCC, Cat# CRL-3216	RRID: CVCL_0063
SH-10-TC [Gastric, RPMI with HEPES, 10% FBS + Nonessential amino acids, Penstrep, L-Glutamine, Sodium Pyruvate, & Vitamins, STR-Confirmed, Mycoplasma negative]	Local: Dr. Andrew S. Brohl, Moffitt Cancer Center, FL, USA; Commercial: JCRB: Cat# RCB1940	RRID: CVCL_5167
UMUC-14 [Bladder, MEM with 10% FBS + Nonessential amino acids, Penstrep, L-Glutamine, Sodium Pyruvate, & Vitamins, STR-Confirmed, Mycoplasma negative]	Local: Drs. Lewis S. Jason, Patricia Manuela Memorial Sloan Kettering Cancer Center, USA, NY, USA; Commercial: Sigma Cat # 08090509	RRID: CVCL_2747
HT-1197 [Bladder, MEM with 10% FBS + Nonessential amino acids, Penstrep, L-Glutamine, Sodium Pyruvate, & Vitamins, STR-Confirmed, Mycoplasma negative]	Local: Drs. Lewis S. Jason, Patricia Manuela Memorial Sloan Kettering Cancer Center, USA, NY, USA; Commercial: ATCC: Cat# CRL-1473	RRID: CVCL_1291
WM793 [Melanoma, MEM with 10% FBS + Nonessential amino acids, Penstrep, L-Glutamine, Sodium Pyruvate, & Vitamins, STR-Confirmed, Mycoplasma negative]	Local: Drs. Keiran S.M. Smalley, Manali S. Phadke, Moffitt Cancer Center, FL, USA; Commercial: ATCC: Cat# CRL-2806	RRID: CVCL_8787
IPC298 [Melanoma, MEM with 10% FBS + Nonessential amino acids, Penstrep, L-Glutamine, Sodium Pyruvate, & Vitamins, STR-Confirmed, Mycoplasma negative]	Local: Drs. Keiran S.M. Smalley, Manali S. Phadke, Moffitt Cancer Center, FL, USA; Commercial: DSMS: Cat# ACC 251	RRID: CVCL_1307
A375 [Melanoma, MEM with 10% FBS + Nonessential amino acids, Penstrep, L-Glutamine, Sodium Pyruvate, & Vitamins, STR-Confirmed, Mycoplasma negative]	Local: Drs. Keiran S.M. Smalley, Manali S. Phadke, Moffitt Cancer Center, FL, USA; Commercial: ATCC: Cat# CRL-1619	RRID: CVCL_0132
Oligonucleotides		
Anti-miR-519D-3p [Usage 30 nM]	Sigma 5′-CACUCUAAAGGGAGGCACUUUG-3′	NA (Custom synthesis)
Anti-miR-519D-5p [Usage 30 nM]	Sigma 5′-AACAGAAAGCGCUUCCCUU UGGAGG-3′	NA (Custom synthesis)
Anti-miR-526B-3p [Usage 30 nM]	Sigma 5′-GCCUCUAAAAGGAAGCACUUUC-3′	NA (Custom synthesis)
Anti-miR-526B-5p [Usage 30 nM]	Sigma 5′-ACAGAAAGUGCUUCCCUCAAGAGG-3′	NA (Custom synthesis)
Non-targeting-CSi000A [Usage 30 nM]	Sigma 5′-Cy5-CGUGCGGGCCCGGGCGUGC-3′	NA (Custom synthesis)
Non-targeting-CSi000B [Usage 30 nM]	Sigma 5′-Cy5-CGUGCGGGGGGCCCCGUGC-3′	NA (Custom synthesis)
Colony PCR-F [5′-TAAAATGGACTAT CATATGCTTACCG -3′] PCR/RT-PCR primers with annealing temperature of 60°C	Product size: 188 bp	Template: Bacterial colony (plasmid: pSpCas9[BB]-2A-Puro [PX459] V2.0)
Colony PCR-R [5′-AACAAAAAAGCA CCGACTCGGTGCC -3′] PCR/RT-PCR primers with annealing temperature of 60°C	Product size: 188 bp	Template: Bacterial colony (plasmid: pSpCas9[BB]-2A-Puro [PX459] V2.0)

(*Continued on next page*)

Continued

REAGENT or RESOURCE	SOURCE	IDENTIFIER
Chop86-F [5′-TTTCGCCCGCTGCCTGGAAG TATC -3′] PCR/RT-PCR primers with annealing temperature of 60°C	Product size: 999 bp if not chopped; Lower size ladder(s) if chopped off; The ladders <999 bp is formed due to variability in 13-repeat knock-out in pooled cells. A single band can be obtained from single cell clones.	Template: Human genomic DNA
Chop86-R [5′-CCGATTCTCCCACCTCAGCC TCCC -3′] PCR/RT-PCR primers with annealing temperature of 60°C	Product size: 999 bp if not chopped; Lower size ladder(s) if chopped off ; The ladders <999 bp is formed due to variability in 13-repeat knock-out in pooled cells. A single band can be obtained from single cell clones.	Template: Human genomic DNA
SpCas9-F [5′-TTCTGGCGGTTCTCTTCAGC CGGG-3′] PCR/RT-PCR primers with annealing temperature of 60°C	Product size: 468 bp	Template: Human genomic DNA of CRISPRed cells.
SpCas9-R [5′-CGGGACGGCCCTTCTCCTCC GGG-3′] PCR/RT-PCR primers with annealing temperature of 60°C	Product size: 468 bp	Template: Human genomic DNA of CRISPRed cells.
IGFBP3-F [5′-GGGCGCGACCCACGCTCTG GGCC-3′] PCR/RT-PCR primers with annealing temperature of 60°C	Product size: 350 bp	Template: Human genomic DNA.
IGFBP3-R [5′-GGCACTAGCGTTGACG CAGAGCCC-3′] PCR/RT-PCR primers with annealing temperature of 60°C	Product size: 350 bp	Template: Human genomic DNA.
Recombinant DNA		
pMIR-CMV-GFP-Puro [Generated stable MCF-7 cells]	Vigene Biosciences	NA
pMIR-CMV-miR-519D-GFP-Puro [Generated stable MCF-7 cells]	Vigene Biosciences	CR215546
pMIR-CMV-miR-526B-GFP-Puro [Generated stable MCF-7 cells]	Vigene Biosciences	CR215142
pEGFP-C1-emerin (EMD); [Generated transient line in WM793 cells]	Dr. Katherine L. Wilson (Department of Cell Biology, Johns Hopkins University School of Medicine, Baltimore, MD 21205, USA)	NA (Gift)
pMRX-IP-GFP-LC3-RFP; [Generated transient line in WM793 cells]	Addgene	84573
Software and algorithms		
Anaconda	https://www.anaconda.com/	Version: Anaconda3-2024.02-1
Python3-Jupyter	https://jupyter.org/	Version: 7.0.8
Python3-Pandas	https://pandas.pydata.org/	Version: 2.1.4
Python3-Seaborn	https://seaborn.pydata.org/	Version: 0.12.2
GraphPad Prism	http://www.graphpad.com/	Version: 7.04
Adobe Photoshop	https://www.adobe.com/	Version: CS5
Leica Biosystems Aperio ImageScope	https://www2.leicabiosystems.com/na/digital-pathology	Version: 12.4.6.5003
ImageJ, NIH, USA	http://imagej.nih.gov/ij	Version: 1.53k
SnapGene viewer	https://www.snapgene.com/snapgene-viewer	Version: 6.0.6
Clarivate EndNote	https://endnote.com/	Version: X9.3.3
IGV; Broad Institute, USA	https://software.broadinstitute.org/software/igv/	Version: 2.12.2
FinchTV; Geospiza	https://digitalworldbiology.com/FinchTV	Version: 1.4.0

(*Continued on next page*)

Continued

REAGENT or RESOURCE	SOURCE	IDENTIFIER
NewTek Lightwave-3D	https://lightwave3d.com//	Version: 10
R studio; Posit	https://posit.co/download/rstudio-desktop/	Version: 2021.09.2 Build 382; "Ghost Orchid" Release for Windows
ggplot2; R studio	https://github.com/tidyverse/ggplot2/tree/main	Version: Built under R version 4.1.3
ggRidges; R studio	https://github.com/wilkelab/ggridges	Version: Built under R version 4.1.3
Microsoft Office-Excel	https://www.microsoft.com/en-us/microsoft-365/microsoft-office	Version: 2021
Microsoft Office-Word	https://www.microsoft.com/en-us/microsoft-365/microsoft-office	Version: 2021
GeneVenn	https://www.bioinformatics.org/gvenn/	Online server
EnrichR	https://maayanlab.cloud/Enrichr/	Online server

EXPERIMENTAL MODEL AND STUDY PARTICIPANT DETAILS

Human subject statement

This study does not deal with human subjects or PHI other than using deidentified TCGA transcriptomics and histology data. The IDs provided in Figure S4D are TCGA-deidentified IDs. The sample size for C19MC^{High} versus C19MC^{Low} patient groupings were done based on the pan-normal C19MC cut-off described in detail below at section: pan-cancer clinical datasets and data processing.

IBC approval

Use of all CRISPR guides were approved by Institutional Biosafety Committee (IBC-University of South Florida: PROTO2022-041) and were used as plasmids instead of viruses.

Cell lines, and constructs

The list of cell lines, and recombinant constructs are given in key resources table titled "Cell lines used in this study, source, authentication, and maintenance" and "List of commercial, gifted and cloned plasmids used in this study". New cloned construct details are given in the CRISPR section of STAR Methods.

METHOD DETAILS

Pan-cancer clinical datasets and data processing

The results in this study are in part based upon the data generated by the TCGA (The Cancer Genome Atlas) Research Network: https://www.cancer.gov/tcga. TCGA miRNA-seq, and RNA-seq, data for all available cancer types [Adrenocortical carcinoma (ACC), Bladder urothelial carcinoma (BLCA), Breast invasive carcinoma (BRCA), Cervical and endocervical cancers (CESC), Cholangiocarcinoma (CHOL), Colon adenocarcinoma (COAD), Rectum adenocarcinoma (READ), Diffuse Large B-cell Lymphoma (DLBC), Esophageal carcinoma (ESCA), Glioblastoma multiforme (GBM), Brain Lower Grade Glioma (LGG), Head and Neck squamous cell carcinoma (HNSC), Kidney Chromophobe (KICH), Kidney renal clear cell carcinoma (KIRC), Kidney renal papillary cell carcinoma (KIRP), Acute Myeloid Leukemia (LAML), Liver hepatocellular carcinoma (LIHC), Lung adenocarcinoma (LUAD), Lung squamous cell carcinoma (LUSC), Mesothelioma (MESO), Ovarian serous cystadenocarcinoma (OV), Pancreatic adenocarcinoma (PAAD), Pheochromocytoma and Paraganglioma (PCPG), Prostate adenocarcinoma (PRAD), Sarcoma (SARC), Skin Cutaneous Melanoma (SKCM), Stomach adenocarcinoma (STAD), Testicular Germ Cell Tumors (TGCT), Thyroid carcinoma (THCA), Thymoma (THYM), Uterine Corpus Endometrial Carcinoma (UCEC), Uterine Carcinosarcoma (UCS), and Uveal Melanoma (UVM)] were from (https://gdac.broadinstitute.org/).

Setting up the C19MC^{High} and C19MC^{Low} groups and integration of miRNASeq and RNA-seq data within each cancer types

Based on the normal (matched, as per TCGA-IDs) samples in all cancer types (excluding a few cancer types which do not have normal samples) we set up a cumulative C19MC miRNA expression cut-off of 48.25 (reads per million) at 98 percentiles of pan-normal C19MC expression. Based on cumulative expression of all 46 C19MC miRNAs 13/33 cancer types (PCPG, MESO, COAD, GBM, KIRC, PRAD, READ, LGG, PAAD, LAML, KICH, ACC, and CHOL) were not subjected to further analyses due to no or low number of tumors with C19MC expression above the C19MC expression cut-off value. The remaining 20 cancer types were classified into C19MC^{High} and C19MC^{Low} groups with equal number of tumors/patients on each group based on the number of tumors available on both extremes of the C19MC expression spectrum.

Integration of miRNA-seq and RNA-seq datasets of 20 cancer types

Based on the C19MC^{High} and C19MC^{Low} group TCGA samples, the barcodes of miRNA-seq datasets were integrated to the RNA-seq datasets of the corresponding cancer type. The patients who do not have RNA-seq data matching to miRNA-seq data or vice versa were omitted and the group size were kept equal accordingly to have equal statistical power during downstream analyses.

C19MC^{High} versus C19MC^{Low} gene set enrichment analyses (GSEAs) and visualizations in R

The data of C19MC^{High} and C19MC^{Low} groups of 20 cancer types that had C19MC expression values above or below the cut-off value were subjected to FPKM adjustment and group averages for all individual genes were calculated. The group averages of individual genes were subjected to GSEA analyses for Hallmark, C1-positional, C2-curated, C3-motif, C5-Gene ontology, C6-Oncogenic and C7-Immunologic complete gene set collections/modules for humans (MSigDB: https://www.gsea-msigdb.org/gsea/msigdb/version 7.2). The phenotypes analyzed were always C19MC^{High} versus C19MC^{Low} tumors and thus the normalized enrichment scores (NES) and FDRq values represent enrichments in C19MC^{High} tumors compared to corresponding C19MC^{Low} tumors. We generated 15060 enrichment results per cancer type and a total of 301,200 enrichments for 20 cancer types (excluding C1 positional set enrichments). All module enrichment results were combined for each cancer type to rank enrichments. Top ranked gene-sets (positive and negative NES) with lowest FDRq value in C19MC^{High} tumors of each cancer type is tracked across all 20 cancer types irrespective of the enrichment status in remaining cancer types. Dot plots were generated in R using ggplot2 package[34] (R version 4.1.3). NES and FDRq values categorized based on functional groups and enrichment across more cancer types for further downstream investigations. Currently, we excluded immune signatures except a few, as this study focuses on a cell biological phenomenon. FDRq values were converted to negative integers so as to reflect the dot size smaller for false discoveries, but labelled in positive values. For all TCGA 20 cancer type GSEA enrichment dot plots, the NES and FDRq scales were kept constant (-3.5 to 3.5 for NES and 0 to 1 for FDRq), so that one can compare an enrichment with any other TCGA 20 cancer dot plot in this study.

Certain signatures were tracked even though if it is not coherently enriched in C19MC^{High} cancers as knowing its status was important to shed light on the biological context. For example, ESCRT versus APC signatures in Figure S2H.

R CODE

```
> ggplot(DFname, aes(x = CancerTypeNES, y = Geneset)) +
   geom_point(aes(size = NegFDRq, color = NES)) +
   geom_point(shape=0, size=12)+
   scale_color_gradientn(colours = c("greenyellow", "green2", "black", "red", "yellow"),
   limits = c(-3.5, 3.5),
   breaks = c(-3.00, -2.00, -1.00, 0, 1.00, 2.00, 3.00))+
   theme_classic()
   # Limits kept constant for all TCGA dot plots as it encompasses the data range of NES.
```

CCLE 954 cell line cumulative C19MC expression analysis

Cancer Cell Line Encyclopedia (CCLE: https://sites.broadinstitute.org/ccle/) miRNASeq data were processed for cumulative expression of all 46 C19MC miRNAs (miR498, miR512-1, miR512-2, miR515-1, miR515-2, miR516A1, miR516A2, miR516B1, miR516B2, miR517A, miR517-B, miR517C, miR518A1, miR518A2, miR518B, miR518C, miR518D, miR518E, miR518F, miR519A1, miR519A2, miR519B, miR519C, miR519D, miR519E, miR520A, miR520B, miR520C, miR520D, miR520E, miR520F, miR520G, miR520H, miR521-1, miR521-2, miR522, miR523, miR524, miR525, miR526A1, miR526A2, miR526B, miR527, miR1283-1, miR1283-2, and miR1323)[15] and plotted in GraphPad Prism software to get an insight into the C19MC^{High} cell lines. Of note, WM793 is one of the top C19MC^{High} cell line (Figure S2E).

CCLE 1020 cell line IAV, HIV, and shared signature analysis

Influenza-A virus (IAV) infection and HIV infection signatures were obtained from MSigDB. Both signatures were fed into GeneVenn (https://www.bioinformatics.org/gvenn/) to get unique (IAV-specific and HIV-specific) and shared genes of these signatures. Cancer Cell Line Encyclopedia (CCLE: https://sites.broadinstitute.org/ccle/) RNA-seq data were processed for IAV-specific, HIV-specific and shared gene set cumulative averages and plotted in GraphPad Prism software (Figure S2B).

dbGAP data access and IGV visualization of C19MC transcriptional landscape

Cancer Cell Line Encyclopedia (CCLE) RNA-seq C19MC^{High} cell line data and NIH database of Genotypes and Phenotypes (dbGAP: The results published here are in part based upon data generated by The Cancer Genome Atlas managed by the NCI and NHGRI. Information about TCGA can be found at http://cancergenome.nih.gov). TGCT C19MC^{High} patient RNA-seq data BAM files were visualized for C19MC transcriptional landscape at C19MC locus using integrated Genomics Viewer.[35] While different transcriptional starts were noted, we focused on the start site at CpG86 location that matched WM793 cells (Figure S3A). The zoom in feature was used to locate the precise

start site, which matched to the CpG86 13-repeat sequence region. The CpG island ID: 86 was as per UCSC Genome Browser nomenclature (HG19).

EnrichR analyses

Critical gene signatures enriched in TCGA datasets such as meiosis and influenza signatures were filtered for enriched genes in C19MC^{High} tumors such as TGCT and fed into EnrichR[36–38] to find matching cell lines either in NCI-60 cell line panel or in proteomics based CCLE database. Enrichments results such as adjusted p-value and combined score were plotted in R using ggplot2 package[34] (R version 4.1.3).

R CODE

```
> ggplot(DFname, aes(x = Group, y = CellLine)) +
   geom_point(aes(size = AdjPvalue, color = CombinedScore)) +
     geom_point(shape=0, size=10)+
   scale_color_gradientn(colours = c("black", "red"),
   limits = c(0, 250)) +
   theme_classic()
   # Limits will change according to the data range.
```

Bird's eye view volcano plot: Meiotic-regulatory gene expression in C19MC^{High} groups of TGCT vs. THYM

To gain knowledge on the genes that are coregulated and differentially regulated in C19MC^{High} vs. C19MC^{Low} tumors of two prominent C19MC^{High} cancer types (TGCT vs. THYM) the RNA-seq C19MC^{High} and C19MC^{Low} dataset genes were subjected to average and subsequent log2 fold change (L2FC) calculations. The log2 fold change data were subjected to XY volcano plotting in GraphPad Prism, with lines demarking the log2 fold change level of 2 or -2 on each axis. The quadrant that represents genes that are upregulated in C19MC^{High} THYM as well as in C19MC^{High} TGCT were examined for meiotic regulatory genes. *CGA* and *CGB1* RNAs corresponding to the protein heterodimers of the meiotic-regulatory pregnancy hormone human chorionic gonadotrophin (hCG)[27] was marked in Figure S2M.

Cell lines: Authentication, quality control and maintenance

Human cancer cell lines (listed in the key resources table titled "Cell lines used in this study, source, authentication, and maintenance") were obtained, cultured at 37°C with 5% CO2 in MEM (Sigma: M4655)/RPMI 1640 (Hyclone #SH30255FS) supplemented with L-Glutamine (Gibco Life Technologies # A2916801), vitamins (Gibco Life Technologies #11120052), sodium pyruvate (Gibco Life Technologies #11360070), non-essential amino acids (NEAA: Gibco Life Technologies #11140050), penicillin-streptomycin (Gibco Life Technologies #15140122) with 10% FBS (Sigma#F0926). The cells were DNA fingerprinted and periodically tested for Mycoplasma as described previously.[16,17]

Chemical reagents/inhibitors and usage

A list of chemical agents used in this study are provided in the key resources table titled "Chemical agents used in this study".

Protein hormone, enzymes, kits, antibodies, transfection reagents and usage

A list of protein and antibody reagents used in this study are provided in the key resources table titled "List of protein and antibody reagents used in this study".

Genetic reagents (anti-miRNAs, RNA-probes)

A list of anti-miRs and RNA-probes used in this study are provided in the key resources table titled "List of custom anti-miRs and RNA-probes used in this study".

Genetic reagents (plasmid DNAs) and stable cell lines generated: No viruses

A list of plasmids used in this study are provided in the key resources table titled "List of commercial, gifted and cloned plasmids used in this study". Of note, usage of viruses was averted throughout the study as the objective is to study the regulation and function of anti-viral response cluster C19MC in the absence of exogenous viruses.

CRISPR guide RNA cloning and Sanger sequencing

The C19MC upstream CpG86 13-repeat knock-out CRISPR guides (Choppers) were cloned as described.[29] Briefly, the Addgene plasmid pSpCas9(BB)-2A-Puro (PX459) V2.0 was digested with BbsI restriction enzyme to release the non-targeting part of the sgRNA, linear vector is gel purified, quantified, and custom synthesized and annealed oligo duplexes of chopper-1 and chopper-2 with suggested overhangs were ligated using Rapid ligation kit but using overnight incubation at 4°C. The ligated plasmids were transformed into DH5α competent cells with

SOC medium recovery and plating as per standard procedures. Individual colonies were picked, screened by colony PCRs with parallel inoculation for glycerol stock preparation in Ampicillin LB broth. Positive colonies were subjected to glycerol stock preparation, plasmid miniprep and Sanger sequencing (Genewiz/Azenta, USA) using individual "Colony PCR" primers (key resources table titled "List of custom PCR primers used in this study"). Plasmids were confirmed for incorporation of oligonucleotide inserts and then subjected to plasmid MIDI prep and quantified before transfections.

CRISPR genetic engineering of CpG86

WM793 cells which has transcription start from the CpG86 13-repeat region through C19MC similar to C19MC^{High} TGCTs (Figure S3A). Therefore, WM793 cells were transfected with pSpCas9(BB)-2A-Puro (PX459) V2.0 (has inbuilt SpCas9) or with CRISPR-choppers 1 and 2 constructs (have inbuilt SpCas9 plus chopper-guides targeting the 13-repeat regions of CpG86 for knock-out; Figure 3A and key resources table titled "List of commercial, gifted and cloned plasmids used in this study") using Lipofectamine-2000 as per manufacturer's protocol with minor modifications (See transient transfection section below). Parental WM793 cells were maintained in parallel to have it as a control. Transfected cells were stably selected using gradual increase of puromycin from 0.5 μg/ml to 4 μg/ml. Upon reaching confluency in transfected cells, the cells were trypsinized and plated for genomic DNA isolation and freezing. Genomic DNA was isolated from parental cells, NGP (Nontargeting-Guide-sgRNA pooled stable cells), and Choppers (Choppers-1 and 2 co-transfected stable pooled cells) and quantified using Nanodrop. 150 ng of genomic DNAs were subjected to CRISPR screening PCR using "Chop86" primers (key resources table titled "List of custom PCR primers used in this study") and the laddering of amplicons in choppers with size <999 were confirmed to have undergone repeat deletions and fusion of flanking ends, as the primers bind outside PAM sites and the 13-repeat region.

Sanger sequencing of CRISPRed genomic regions

To confirm that the CRISPR-choppers indeed deleted the repeat region, Chop86 primer (key resources table titled "List of custom PCR primers used in this study") -directed DNA amplicons from genomic DNA of WM793-choppers cells were subjected to TA-cloning in pGEM-T Easy vector system and minipreps of plasmids were subjected to Sanger sequencing (Genewiz/Azenta, USA) using individual "Chop86" primers (key resources table titled "List of custom PCR primers used in this study"). We confirmed that the choppers-1 and 2 resulted in the knock-out of 10 out of 13 repeats within the CpG86 upstream of C19MC (Figures 3A and S3C).

CpG86: 13-repeat hypervariability test

To examine the repeat numbers within CpG86 (UCSC Genome browser, HG19) that is upstream of C19MC across multiple human cancer cell lines, Chop86 primer (key resources table titled "List of custom PCR primers used in this study") -directed DNA amplicons from genomic DNA of 19 cancer cell lines from various cancer type were subjected to agarose gel electrophoresis. The cell lines exhibited hypervariability in this region as evidenced by high variability in product size (Figure S3B). As it appeared MCF-7 cells had naturally smallest amplicon among all products (Figure S3B) and is of in meiotic interest (See text), we subjected the MCF-7 amplicon by Sanger sequencing (Genewiz/Azenta, USA) using individual "Chop86" primers (key resources table titled "List of custom PCR primers used in this study"). We confirmed that MCF-7 cells naturally lack 8 out of 13 repeats within the CpG86 upstream of C19MC (Figures S3B and S3C).

Genomic DNA CRISPR screening PCRs, colony PCRs and primers

A list of PCR primers used in this study and their reaction conditions are provided in the key resources table titled "List of custom PCR primers used in this study". All PCR reactions were performed with an initial denaturation of 95°C for 3 minutes; cycling conditions of 95°C for 1 minute, 60°C for 30 seconds, 72°C for 1 minute for 34 cycles; and a final extension time of 72°C for 5 minutes. All reactions had a final concentration of 1M betaine.

Transient gene/anti-miR transfections

WM793 cells in 6-well plates (50,000 cells/well, plated 24 hours before) were transfected with 1 μg of pEGFP-C1-EMD (specified in key resources table titled "List of commercial, gifted and cloned plasmids used in this study") using Lipofectamine 2000 as per manufacturer's protocol with minor modifications. Briefly, 300 μl of Opti-MEM was mixed with 5 μl of Lipofectamine 2000 and separately, 300 μl of Opti-MEM was mixed with 1 μg of pEGFP-C1-EMD plasmid and incubated for 5 minutes. Both mixtures were pooled by gradual mixing and incubated further in room temperature for 30-40 minutes. This ~600 μl mixture was added to the media removed cells in a drop-wise fashion, and further 3.5 ml complete MEM was added gently to the cells/well of 6-well plate. 24 hours after, the media was changed again. 48 hours after transfection, cells were imaged for EGFP-emerin expression with or without live nuclear DNA staining using Hoechst-33342.

All anti-miR transfections were done similar to EGFP-emerin transfections, but using RNAiMAX reagent instead of Lipofectamine 2000, and plasmids were substituted with 30 nM anti-miRs. Cy5 labelled non-targeting RNA was used separately to monitor transfection efficiency. 24 hours after transfection, the media was changed with or without treatments as per experiment set-up.

For pMRX-IP-GFP-LC3-RFP plasmid transfection, please see below at section: detection of autophagic flux within sub-cellular locations [Cytoplasmic vs. nucle(ol)ar invasive cytoplasm].

Stable transfections of single C19MC miRNAs and cell sorting

MCF-7 cells in 6-well plates were transfected with 1 μg of pMIR, pMIR-519D and pMIR-526B (viral transduction was averted throughout the study as C19MC is a viral response cluster) using Lipofectamine 2000 as described previously.[17] 48 hours after transfection the cells were selected against gradual doses of puromycin (0.5, 1, 2, and 4 μg/ml each subsequent week) for a period of 2 months, expanded and were sorted (BD FACSAria Cell Sorter) for GFP, and further expanded GFP-positive cells before freezing. The cells were maintained in 4 μg/ml puromycin containing MEM and were switched to puromycin free medium for experiments.

Microscopy

Microscopy was performed as described previously.[16,17] Cells were imaged using Zeiss Observer.Z1 microscope equipped with Axiocam 503 mono (Zeiss) camera. For fluorescence microscopy the individual channel images were pseudo-colored if indicated in figures/legends or imaged in grey scale (for Giemsa cytogenetics), merged, and exported to jpeg using ZEN 2.3 Pro software (Carl Zeiss Microscopy, GmbH, 2011, Blue edition). The final composite was created using Adobe Photoshop CS5 (Adobe Systems Inc., San Jose, CA, USA).

Nucle(ol)ar invasion of cytoplasm [NiC] assays

WM793 cells that constitutively overexpress most of 46 C19MC miRNAs were treated with 20 nM Aurora-B inhibitor (Aurora-Bi: AZD1152-HQPA) or DMSO for 24 hours and were live stained for DNA using Hoechst-33342 for 20 minutes before imaging the cells for Nucle(ol)ar invasion of cytoplasm by evaluating the appearance of large Hoechst-33342-positive-DNA-free area within the nuclei. The nuclear DNA stain images were subjected to nucle(ol)ar invasive cytoplasm 2D area measurement (Dark zone within nuclei) using ImageJ software. The arbitrary area units obtained in ImageJ were converted to square micrometer area unit using a reference scale box of 100 sq. mm. For some experiments arbitrary units were used as such or after down scaling. Three hundred cells (nuclei) from replicates were counted/measured for nucle(ol)ar invasive cytoplasm area/positivity and were plotted in GraphPad Prism software using aligned dot plot (barcode symbol) using the settings of standard error of mean. The data points were displayed with 50% transparency to visualize the overlap density.

To evaluate changes in the size of nucle(ol)ar invasive cytoplasm, meiosis promoters hCG[39] (25 ng/ml), all-trans retinoic acid[18] (ATRA:1μM), and non-lethal doses of IAV+HIV signature inhibitors (Figure S2N) such as actinomycin-D, cycloheximide, MG-132, leptomycin-B, Ro3306 were treated in WM793 cells with or without 20 nM Aurora-B inhibitor (AZD1152-HQPA) for 24 hours, and were stained for DNA using Hoechst-33342 for 20 minutes before live imaging the cells. The counting and or measurement of nucle(ol)ar invasive cytoplasm area were done as described above.

To evaluate the relationship of nuclear DNA replication, nucle(ol)ar invasive cytoplasm area and intensity were measured in addition to Hoechst-33342-poitive DNA area/intensity (Nuclear area/intensity subtracted with nucle(ol)ar invasive cytoplasm area/intensity).

To evaluate the requirement of C19MC to form nucle(ol)ar invasive cytoplasm, CRISPR engineered WM793 pooled cells were used with Aurora-B inhibitor (AZD1152-HQPA) for 24 hours and were stained for DNA using Hoechst-33342 for 20 minutes before imaging the cells. The use of pooled cells eliminates the possibility of clonal effect/drift in nucle(ol)ar invasive cytoplasm phenotype. Nucle(ol)ar invasive cytoplasm area versus nuclear area and DNA intensity results were plotted in R using ggplot2 package[34] (R version 4.1.3). Nuclear area measurements were scaled down by dividing the AU values by 1000 or as indicated in figures (Figure 3E). T-tests were done in Microsoft Excel to calculate the significance.

R CODE

```
> ggplot(DFname, aes(x = MeasurementsNucArea, y = MeasurementsNiCArea)) +
   geom_point(aes(colour= MeasurementsDNAintensity)) +
   scale_color_gradientn(colours = c("black", "red", "yellow"),
   limits = c(0, 70))+
     xlim(0, 20) +
     ylim(0, 4000)+
   geom_rug()+
   theme_bw()
   # Limits kept constant according to the data range of all three cell types.
   # Axis limits set based on the data range of all three cell types combined.
```

Detection of mitochondria within nucle(ol)ar invasive cytoplasm

WM793 cells were plated in 6-well plates (50,000 cells/ml; 4ml/well) and 24 hours after treated with 20 nM Aurora-B inhibitor (AZD1152-HQPA) for 24 hours. 30 minutes before the end of treatment duration, the cells were live stained with JC-1 and Hoechst-33342 before imaging using Zeiss Observer.Z1 microscope. Polarized mitochondria, and DNA were imaged using appropriate filters for red, and blue channels respectively and pseudo-colored as indicated in figures.

Independently, WM793 cells were transfected with 30 nM Cy5-labelled CSi000A RNA probe, and 24 hours after transfection treated with 20 nM Aurora-B inhibitor (AZD1152-HQPA) for 24 hours. 30 minutes before the end of treatment duration, the cells were live stained with Hoechst-33342 before imaging using Zeiss Observer.Z1 microscope. Cy5-CSi000A-RNA-labelled mitochondria, and DNA were imaged using appropriate filters and pseudo-colored as indicated in figures.

Detecting Giemsa positive DNA, and mitochondria within the closed nucle(ol)ar invasive cytoplasm

To understand nucle(ol)ar invasive cytoplasm is a closed compartment or a result of donut like nucleus we decided to isolate the nuclei by hypotonic swelling where cytoplasmic materials will be lost but the nuclear integrity can be retained by restricting the swelling time limited. We combined this strategy to also explore the presence of DNA and mitochondria within the nucle(ol)ar invasive cytoplasmic compartment. Briefly, MCF-7 miR-519D stably transfected cells were plated at a density of 100,000 cells/ml for 24 hours and treated with 20 nM Aurora-B inhibitor for 24 hours in 10% FBS containing MEM. The cells were collected by shake-off plus vigorous pipetting to dislodge cells. The cells were pelleted at 1000 rpm and resuspended with 7 mL of 0.067 mol/L KCl, allowed to swell for 1 minute, fixed (two step: 7 drops and then 7 mL of fresh fixative 3:1 methanol: glacial acetic acid). The cells in fixative were incubated at -20°C overnight, washed with fresh fixative, dropped-in on "+ slides", air-dried, aged for 1 hour at 70°C using a slide warmer (Fisher Scientific), rehydrated and dehydrated using graded series of ethanol, and stained with 2% modified Giemsa stain (PBS, 70% ethanol, 95%ethanol, 3 dips each, air dried, 2% Wright's modified Giemsa staining for 5 minutes, 3 distilled water dips and air dried). The slides were then incubated with 30 nM Cy-5-labelled-CSi000A + 10 nM Hoechst-33342 for 20 minutes at room temperature, and washed with PBS three times. Imaging was done using appropriate filters for Hoechst-33342, Cy-5 or bright field, and image processing was done as described in microscopy section. Nucle(ol)ar invasive cytoplasm was found positive for Giemsa-positive DNA, CSi000A-positive mitochondria and relatively free from Hoechst-33342-positive DNA (Figure S2K).

Quantification of mitochondria traffic into the nucle(ol)ar invasive cytoplasmic compartment and visualization in R

WM793 parental cells, WM793-NGP cells (CRISPR-control with SpCas9 stably transfected), and WM793-CRISPR-CpG86-engineered choppers cells (Choppers-1 and 2 with SpCas9 stably transfected and Sanger sequence confirmed) were plated in puromycin free complete MEM at a density of 50,000 cells/ml; 4ml/well of 6-well plate for 24 hours. The cells were then treated with 20 nM Aurora-B inhibitor (AZD1152-HQPA) and 30 nM Cy5-CSi000A (not using transfection reagent) for 24 hours and protected from light from this step onwards. 30 minutes before the end of treatment duration, the cells were live stained with Hoechst-33342 before imaging using Zeiss Observer.Z1 microscope. Exposure times for each channel were kept constant between conditions. Hoechst-33342 and Cy5-CSi000A channels were exported individually as well as merged and subjected to quantification of nuclear DNA and mitochondria within nucle(ol)ar invasive cytoplasm using ImageJ. While most of WM793-NGP cells do not form nucle(ol)ar invasive cytoplasm, a small free-hand tool dot was drawn (<100 arbitrary unit [AU] in Figure 3H) inside nuclei to get a measurement for a data point. To nullify this in CSi000A-labelled mitochondria at nucle(ol)ar invasive cytoplasm, we introduced a generous gate at 25 scaled down AU (corresponding original AU is 250) on X-axis (green dotted line in Figure 3H) and compared the mitochondria influx over 25 scaled down AU between CRISPR-CpG86-engineered cells versus NGP or parental cells. A $\log_{10}$ ratio of nuclear DNA (Hoechst-33342 positive) to CSi000A-labelled mitochondria at nucle(ol)ar invasive cytoplasm were calculated to evaluate the relationship of nuclear DNA content to NiC invasion of mitochondria. The CSi000A intensity was scaled down by dividing the intensity AU values by 10. Mitochondria traffic into nucle(ol)ar invasive cytoplasm results were plotted in R using ggplot2 package[34] (R version 4.1.3). The gate was introduced in Adobe Photoshop CS5, and the percentage calculations based on gate values were done using Microsoft Excel. T-tests were done in Microsoft Excel to calculate the significance.

R CODE

```
> ggplot(DFname, aes(x = CSi000AintensityAtNiC, y = NiCAreaAU)) +
   geom_point(aes(colour= L10nDNAtoNiCCSi000ARatio)) +
   scale_color_gradientn(colours = c("black", "red", "olivedrab1", "yellow"),
   limits = c(0, 3.5))+
   geom_rug()+
   theme_bw()
   # Limits kept constant according to the data range of all three cell types.
```

Immunofluorescence

SYCP2

Immunofluorescence was performed as described previously.[40,41] Briefly, stable MCF-7-pMIR (GFP expressing), MCF-7-miR-519D (GFP expressing), MCF-7-miR-526B (GFP expressing), WM793 parental cells, CRISPR-Cas9 control-NGP pooled cells, and CRISPR-CpG86-engineered WM793 choppers pooled cells were plated in 24 well plates at 50,000 cells/ml and cultured for 48hrs with a media change at

24hrs. The cells were fixed in ice- cold methanol at -20°C for a period of 24-48hrs. The cells were then washed with PBS, blocked for 30 minutes at room temperature using 300 µl blocking buffer/well (1% BSA and 0.3% Triton-X100 in PBS). The cells were then incubated overnight with SYCP2 antibody (Sigma, HPA062401: Dilution 1:250) in blocking buffer. The cells were washed and incubated with F(ab)2-goat anti-rabbit IgG (H+L) labelled with Alexa fluor-555 or Cy5 (1:1000 dilution in blocking buffer) for 1 hour at room temperature while protected from light. The cells were washed with PBS thrice and incubated with 10 nM Hoechst-33342 in PBS (Sigma) for 20 minutes, and imaged. Exposure times for each channel were kept constant between conditions. The total fluorescence signal per frame was quantified using ImageJ and the number of cells were counted to calculate average SYCP2 intensity/cell/frame. Six such random frames were quantified and the data were plotted as aligned dot plot with standard error of mean in GraphPad Prism software.

β-Tubulin

Immunofluorescence for β-Tubulin was performed similarly in WM793 cells treated with 20 nM Aurora-B inhibitor for 24 hours (to generate nucle(ol)ar invasive cytoplasm), but with goat anti-mouse IgG (H+L) cross-adsorbed secondary antibody labelled with Cyanine-5 (1:1000 dilution in blocking buffer). Quantification was not performed as >90% of cells lacked β-Tubulin expression except small clusters of cells. Therefore, MTOC positive for β-Tubulin invasion into nucle(ol)ar invasive cytoplasm is qualitative (Figure S3F).

Nucleolin/C23, RPS6, REST/NRSF

Please see the section: quantification of nucleolin, RPS6, REST/NRSF traffic into the nucle(ol)ar invasive cytoplasmic compartment and visualization in R.

Quantification of nucleolin, RPS6, REST/NRSF traffic into the nucle(ol)ar invasive cytoplasmic compartment and visualization in R

WM793 parental cells or CRISPR-engineered WM793 cells in parallel to WM793 CRISPR control NG cells were treated with or without Aurora-B inhibitor and or CDK1 inhibitor Ro3306 (as indicated in the figures) for 24 hours, fixed and processed for immunofluorescence of nucleolin, RPS6, REST/NRSF as described above with appropriate Cy5 labelled secondary antibodies. The cells after final wash were incubated with 10 nM Hoechst-33342 in PBS for 20 minutes, and imaged. The immunofluorescence signals within nucle(ol)ar invasive cytoplasmic regions were marked with the aid of Hoechst-33342 DNA image and quantified for area and intensity per nucle(ol)ar invasive cytoplasm/cell. Of note, a small pool of RPS6 and nucleolin are always present within nuclei as part of original nucleolus and ribosome biogenesis process, even in the absence of visible nucle(ol)ar invasive cytoplasm formation (Hoechst-33342 DNA-free regions within nucleus). To nullify this pool, a gate was applied (green dotted line) that matches to the baseline pool of nucleolin and RPS6 at conditions that do not form nucle(ol)ar invasive cytoplasm (WM793-NGP cells) (Figures 3F and 3G). Exposure times for each channel were kept constant between conditions. The nucle(ol)ar invasive cytoplasm immunofluorescence data from 300 individual cells for each condition from replicates were quantified in addition to area, and were plotted in R using ggplot2 package[34] (R version 4.1.3). The gates were introduced in Adobe Photoshop CS5, and the percentage calculations based on gate values were done using Microsoft Excel.

R CODE

```
> ggplot(DFname, aes(x = NiCimmunofluorescence, y = NiCAreaAU)) +
   geom_point(aes(colour= NiCintensityVsAreaRatio)) +
   scale_color_gradientn(colours = c("black", "red", "yellow"),
   limits = c(0, 60))+
     xlim(0, 250) +
     ylim(0, 10000)+
   geom_rug()+
   theme_bw()
   # Limits kept constant according to the data range of all three cell types.
   # Axis limits were based on the range of measurements in all three cell types.
```

Alternatively, the data were plotted in GraphPad Prism software as aligned dot plot with standard error of mean. Data points were given 75% transparency to show the data dense regions (Figures 2L and 2M). T-tests were done in Microsoft Excel to calculate the significance.

Detection of autophagic flux within sub-cellular locations [Cytoplasmic vs. nucle(ol)ar invasive cytoplasm]

Autophagic flux was monitored within subcellular locations using pMRX-IP-GFP-LC3-RFP (Addgene: 84573, was a gift from Dr. Noboru Mizushima, Department of Biochemistry and Molecular Biology, The University of Tokyo, Japan) construct.[32] Briefly, WM793 cells were transiently transfected with pMRX-IP-GFP-LC3-RFP plasmid followed by selection for 2 weeks. The cells were then plated at 50, 000 cells/ml density for 24 hours in complete medium and then treated with 20 nM Aurora-B inhibitor (AZD1152-HQPA) in complete MEM for 24 hours. 30 minutes

before the end of treatment duration, the cells were live stained with Hoechst-33342 before imaging using Zeiss Observer.Z1 microscope. Exposure times for GFP and RFP channels were kept constant. For WM793 cells, GFP fluorescence was detected in live cells and RFP was detected only in dying cells (RFP was constitutively degraded in live cells) therefore, GFP fluorescence was tracked to monitor autophagic flux within subcellular locations. As we compare GFP intensity within subcellular locations within single cells (Figure 4C), the internal control RFP is not required. We refrain from comparing the autophagic flux between cells or between conditions because, the internal control RFP is constitutively degraded in WM793 cell system. Notably, RFP is degraded but not GFP in most of the cells therefore a cleavage between RFP and GFP-LC3 is evident, presumably by ATG4 of autophagy pathway[32] (Figure S4A).

Starvation-induced autophagy, autophagy inhibition experiments, and data visualization in R

WM793 cells that constitutively overexpress C19MC in a cluster-wide fashion (Figures S2D–S2F) were plated in 6-well plates at a density of 50,000 cells/ml, 4ml/well (200,000 cells/well). At 24 hours after plating, the cells were subjected to Aurora-B inhibition (20 nM for 24 hours) or vehicle DMSO, with or without starvation (withdrawal of fetal bovine serum and NEAA+L-glutamine amino-acid supplement). Non-starved cells are considered fed, and labelled as fed cells (Figure 4A). The cells were live stained with 10 nM Hoechst-33342 in existing media for 20 minutes, and imaged with constant exposure time settings. Using ImageJ software, nuclear area (excluding nucle(ol)ar invasive cytoplasm area), Nuclear DNA intensity (Hoechst-33342 positive area intensity, excluding intensity from nucle(ol)ar invasive cytoplasm area), and nucle(ol)ar invasive cytoplasm area were measured for individual cells. The data were plotted in R using ggplot2[34] and ggridges[42] packages (R version 4.1.3).

R CODE

```
#For DNA intensity
  > ggplot(DFname, aes(x = `DNA intensity`, y = Group, fill = stat(x))) +
  xlim(0, 80)+
  scale_y_discrete(expand = c(0, 0)) +
    geom_density_ridges_gradient(scale = 2, rel_min_height = 0.005) +
    scale_fill_gradientn(colours = c("yellow", "red", "black"),
           values = scales::rescale(c(0, 17.5, 35, 52.5, 70))) +
  theme_bw()
  # Axis limits were based on the range of measurements.
  # DF headers, axis limits, and rescale were changed in the above code for nuclear size and NiC size plots.
```

No visual cell death signs were observed at 24 hours of time point under starvation conditions but resulted in the suppression of DNA synthesis (Figure 4A). This suppressed DNA intensity was considered the stage corresponding to G_1 stage of the cell cycle [the DNA intensity equivalent of 18 x 10,000 AU (ImageJ arbitrary units)] (Figure 4A). The dotted lines marking G_1 and G_2 phases were introduced in Adobe Photoshop CS5, and the percentage calculations based on dotted line values and t-test for significance were done using Microsoft Excel. Gates were set at 85 (for nuclear size) and at 200 (for nucle(ol)ar invasive cytoplasm) that discriminates the Aurora-B inhibited conditions from starvation conditions in nuclear and nucle(ol)ar invasive cytoplasm sizes respectively (Figure 4A).

For autophagy inhibition experiments evaluating nucle(ol)ar invasive cytoplasm (Figure 4B), WM793 cells were plated in complete MEM (fed) for 24 hours, and were treated with or without 20 μM chloroquine (CQ) for 24 hours. Nucle(ol)ar invasive cytoplasm size (2D area) was measured as described above using ImageJ software. The data were plotted in R using ggplot2[34] and ggridges[42] packages (R version 4.1.3).

R CODE

```
> ggplot(DFname, aes(x = `NiCArea`, y = Group, fill = stat(x))) +
  xlim(-100, 600)+
  scale_y_discrete(expand = c(0.5, 0.5)) +
    geom_density_ridges_gradient(scale = 1, rel_min_height = 0.0001) +
    scale_fill_gradientn(colours = c("yellow", "red", "black"),
           values = scales::rescale(c(0, 150, 300, 450, 600))) +
  theme_bw()
  # Axis limits were based on the range of measurements.
```

A gate was set at 100, that discriminates the nucle(ol)ar invasive cytoplasm size of Aurora-B inhibited conditions from chloroquine + Aurora-B inhibited conditions to show that the inhibition of autophagy by CQ increases the nucle(ol)ar invasive cytoplasm size (Figure 4B).

Western immunoblotting

Western immunoblotting was done as described previously.[40,43] Briefly, CRISPR-engineered cells in addition to parental control WM793 cells were plated at equal density of 50,000 cells/ml puromycin free complete MEM in 10 cm dishes (10ml/dish). The cells were given a media change at 24 hour and after further 24 hours the cells were lysed using whole cell lysis buffer, and clarified by centrifugation at 13,000 rpm for 10 minutes at 4°C. The clarified lysates were quantified using Bradford assay with reference to bovine serum albumin (BSA). 20 μg lysates per lane were resolved in 10% or 8% SDS-polyacrylamide gels, transferred to nitrocellulose membranes overnight at 40V. The membranes were washed with PBS-Tween20 (PBST), blocked with 5% non-fat dry milk in PBST, and probed with SpCas9 antibody. The bands were visualized with Li-COR system using a secondary antibody compatible with Li-COR system. The membranes were then re-probed with REST/NRSF antibody (Figure 3B).

Tracking proteasomal degradation of SpCas9

Western blotting

To check whether SpCas9 is degraded by proteasomes or autophagy, WM793-NGP cells and WM793-CpG86 choppers CRISPR engineered cells were plated as described above in western immunoblotting section. At 24 hours of plating the cells were treated with or without 1 μM MG-132 or 20 μM CQ for 24 hours. Remaining procedures were performed as described above with the modification that; an 8% SDS-PAGE gel was used to have a better resolution of high molecular weight (HMW)-spCas9 instead of 10% gel (Figure 3C).

Immunofluorescence

To visualize the localization of HMW-SpCas9 in WM793-CpG86-CRISPR-choppers engineered cells, and in WM793-NGP cells, both cells were plated in 24-well pates at a density of 50,000 cells/ml/well. At 24 hours of plating, the cells were treated with 1 μM MG-132 for 24 h and subjected to SpCas9-immunofluorescence as per the immunofluorescence and imaging protocol described above with Hoechst-33342 staining.

Quantification of SpCas9 localization

As we noted a perinuclear distribution of HMW-SpCas9 in MG-132 treated WM793-CpG86-choppers cells, which is different from MG-132 treated control NGP cells where SpCas9 show cytoplasmic localization, we counted the cells with perinuclear versus cytoplasmic SpCas9 distribution. We added more categories such as nucle(ol)ar invasive cytoplasm localized [rare, as MG132 blocks nucle(ol)ar invasive cytoplasm formation in most cells and Aurora-B inhibitor was not used], nuclear localized SpCas9 and so on (Figure S3E).

Cytogenetics: structural chromosomal instability

Cytogenetic procedures were performed as described previously with minor modifications.[6] Briefly, cells were plated at a density of 100,000 cells/ml for 24 hours and treated with 20 ng/ml Colcemid for 16 hours in 10% FBS containing MEM. The mitotic cells and meiotic division-II/III cells that exhibit rounded off/poorly attached morphology were collected by mitotic shake-off method and pelleted at 1000 rpm. The pellets were resuspended with 7 mL of 0.067 mol/L KCl, allowed to swell for 2 minutes, fixed (two steps: 7 drops, and then 7 mL of fresh fixative 3:1 methanol: glacial acetic acid as described previously[44]). The cells in fixative were incubated at -20°C overnight, washed with fresh fixative, subjected to chromosome spreading by high drop-in on "+ slides", air-dried, aged for 1 hour at 70°C using a slide warmer (Fisher Scientific), rehydrated and dehydrated using graded-series of ethanol, and stained with 2% modified Giemsa stain using CTG banding technique with modifications omitting trypsinization step (PBS, 70% ethanol, 95%ethanol, 3 dips each, air-dried, 2% Wright's modified Giemsa staining for 5 minutes, 3 distilled water dips and air-dried). Imaging was done using 40x objective and image processing was done as described in microscopy section. Structural alterations such as meiotic-bridged-chromosomes (MBCs) were considered as structural chromosomal instability.

We observed numerous meiotic bridged-chromosomes (MBCs) in miR-519D transfected stable cells which causes clumped chromosome tangles rather than spread chromosomes (despite adjacent cells were well spread, ruling out the possibility of variations in chromosome spread prep., as well as hypotonic swelling issues). The MBCs exhibit T-type bridges frequently than the X-type bridges to form the network using aberrant DNA-repair mechanism. X-type bridges could indicate the failure to resolve Holliday-junctions, or centromeric non-disjunction due to separase failures. Separase defects and non-disjunction in lagging chromosomes are frequently observed in C19MC miRNA overexpressed MCF-7 cells compared to MCF-7-pMir control cells (Figure S1L).

Cytogenetics: numerical chromosomal instability (nCIN)

As miR-519D overexpressed MCF-7 cells exhibited structural genomic instability (MBCs) which poses hurdles in measuring numerical chromosomal instability (please see previous section), we adapted counting individual chromosomes in cells that do not exhibit MBCs. Cytogenetic procedures were performed as described previously with minor modifications[6] as described above in cytogenetics: structural chromosomal instability section. 25 clean chromosomal spreads (without MBCs) were counted for chromosome numbers and were plotted as mean chromosomal number with standard error of mean using GraphPad Prism software (v7.04; La Jolla, CA, USA). Statistical significance was calculated using student's t-test in Microsoft excel. Numeric alterations compared to control were considered as numeric chromosomal instability (Figure S1N). The experiments were performed at ~2 months of maintenance after obtaining stable cells, to give an idea of timeline for the chromosomal gains in MCF-7-miR-519D cells.

Meiotic nuclear division imaging of isolated nuclei

Cells were plated at a density of 100,000 cells/ml for 24 hours and treated with 20 ng/ml Colcemid for 16 hours in 10% FBS containing MEM to arrest the cells in chromatin condensed state. The cells exhibiting meiotic reduction division-I (Figure 1C) with dumb-bell shaped nucleus exhibits rounded off morphology to a lesser-degree compared to mitotic cells, therefore these cells were collected by mitotic shake-off combined with extensive pipetting of the monolayer cells to dislodge relatively loosely attached cells undergoing meiotic nuclear division. The cells in media were then pelleted at 1000 rpm, pellets were resuspended with 7 mL of 0.067 mol/L KCl, allowed to swell for 1 minute (instead of 2 minutes time used for chromosome prep.), fixed [Step-1: 7 drops of fixative in hypotonic KCL solution and pelleted down at 1000 rpm, Step-2: removed the supernatant and resuspend the pellet in 7 mL of fresh (fixative 3:1 methanol: glacial acetic acid) and pelleted down at 1000 rpm]. The nuclei in fixative were incubated at -20°C overnight, washed with fresh fixative, dropped onto "+ slides", air-dried, aged for 1 hour at 70°C, and stained with 2% modified Giemsa stain as described above. Imaging was done using 40x objective and image processing was done as described in microscopy section. Structural alterations in nuclei such as dumb-bell shaped, sickle-shaped nuclei (often lost the sickle shape to the most part by swelling), and MBC-derived mini-bridged nuclei were imaged (Figure S1M).

Evaluation of DNA content reduction during meiotic nuclear division among daughter nuclei

To understand whether the meiotic nuclear division results in the reduction of genomic DNA content (if the cells have DNA replication preceded by nuclear division, it may not result in potential haploid DNA content as in original meiosis) MCF-7 cells stably overexpressed with C19MC miRNAs 519D, 526B or its control pMIR were live stained with Hoechst-33342. The cells were imaged using constant exposure settings. Individual nuclei, even though the nuclei may reside within single mother cells, were measured for DNA intensity using ImageJ. Measurements from replicates were pooled to have the total spectrum of genomic content difference between individual nuclei and plotted as aligned dot plot in GraphPad Prism software. To gain insight into the density distribution, the same data were subjected to density analysis with same axis parameters in Python within Anaconda navigator-Jupyter/Seaborn/Pandas environment/packages. Finally, both aligned dot plot and density plot were composited in Adobe Photoshop CS5 matching the axis grids (Figure S1O).

ANACONDA/PYTHON CODE

```
[1]: import seaborn as sns
[2]: import pandas as pd
[3]: df=pd.read_csv('DataFileName.csv')
[4]: sns.set_style("whitegrid")
g=sns.displot(kind='kde', data=df, x='DaughterNucDNAintensity',
hue='Group',
fill=True, linewidth=0,
palette = ["#8d02f7", "#030000", "#fa0207"],
legend=False)
g.set(xlim=(-50, 350))
# Plots with and without legends were generated using True/False arguments to identify the peak color associated with data
groups.
```

Nocodazole/Colchicine arrest and release of Meiosis-III cells

To understand the nuclear status of daughter cells derived from Meiosis-III, we isolated Meiosis-III cells from MCF-7 cells by treating them with nocodazole or Colcemid for 16 hours followed by mitotic shake-off procedure described above. Of note, this will also include mitotic cells. The cells were washed twice in 37°C PBS and plated in fresh complete MEM (Nocodazole/Colcemid release), incubated in 5% CO_2 and 37°C, and observed the cells at 30-minute intervals. At 2 hours post release, we found the appearance of daughter cells after ESCRT-cut of the midbodies to find that the daughter cells inherit two nuclei where one is sickle shaped with irregular chromatid condensation to give a hazy appearance with bright spots, whereas the other nuclei show well condensed individual chromosomes (Figure S1C).

To understand the nuclear status of meiotic cells under inhibition of midbody abscission, we isolated meiotic cells from WM793 cells by treating them with nocodazole for 16 hours followed by mitotic shake-off procedure described above. Of note, this will also include mitotic cells. The cells were washed twice in 37°C PBS and plated in fresh complete MEM with 20 nM Aurora-B inhibitor (Nocodazole release but inhibiting midbody abscission), and observed the cells at 2 hours post treatment. Bright field imaging was done to confirm the single cell status. Single cells arrested at meiotic nuclear division (MND) stage with nucle(ol)ar invasive cytoplasm were observed (Figure S2J).

Well-differentiated vs. Poorly-differentiated colony counts

MCF-7 cells stably transfected with C19MC miRNAs 519D, 526B or its control pMir, were plated at the density of 50,000 cells/ml in 6-well plates, with 4 ml puromycin free MEM/well. At 24 hours of plating, the cells were given a round of media change and incubated in 37°C

incubator for another 24 hours with 5% CO_2. The cells were then imaged at bright-field settings to count the colony morphology. A colony with both poorly-differentiated and well-differentiated mixture is counted as poorly-differentiated if more than 50% cells show poorly-differentiated morphology. Alternatively, if a colony shows more than 50% of its cells with well-differentiated morphology, then it is counted as well-differentiated colony. The counts were plotted in GraphPad Prism software with standard error of mean (Figure S1K).

Nuclear counts in living cells

Stable pMIR, p519D or p526B transfected MCF-7 cells or WM793 cells were plated at a density of 50,000 cells/ml puromycin free MEM for 24 hours. At 24 hours, a round of media change was given and further incubated for 24 hours. The cells were then live stained with 10 nM Hoechst-33342 nuclear DNA stain for 20 minutes and were imaged for counting. Bright-field observation is made to ensure 4-daughter nuclei of Meiosis-III and are not counted as 4 instead of 1 cell with sickle nuclei/meiotic nuclear division (Figures 1E and 2A).

Embryonic nuclear division (END) visualization in living cells

MCF-7-pMir, MCF-7-miR-519D, and MCF-7-miR-526B stable cells were plated at a density of 50,000 cells/ml in 6-well plates for 24 hours in puromycin free complete MEM. The cells were transfected with 30 nM of Cy5-CSi000A using RNAiMAX reagent for overnight as described above. 24 hours after removal of transfection components, the cells were live stained with 10 nM of Hoechst-33342 for 20 minutes and imaged for Cy5 and Hoechst-33342 with bright field. The embryonic nuclear division (END) always located within potential cytoplasmic vacuoles (Figures 1G, 1H and S1I) by engulfment of daughter cells through entosis (Figure S1H). END was frequently observed in MCF-7-miR-519D stable cells. Embryonic nuclear division is surrounded by sickle/sickle-nucleated cells both *in vivo* and *in vitro* (Figures S1I and S1J). Embryonic nuclear division also happens as a result of nucle(ol)ar invasive cytoplasm that aids mitochondria mixing with Giemsa stainable DNA (heterochromatin) as embryonic nuclear division and meiotic nuclear division are observed together more frequently (Figure S1I; Figures 1G and 1H).

Metal response stimulation of endogenous C19MC miRs

We previously found that zinc chloride promotes C19MC miRNAs.[17] To examine the role of endogenous C19MC miRNAs in sickle nuclei formation, we generated zinc-resistant MCF-7 cells. Briefly, 200,000 MCF-7 cells/4ml MEM were plated in 6-well plates for 24 hours and at 24-hour timepoint, treated with 1 mM $ZnCl_2$ for 24 hours to eliminate zinc sensitive cells. Remaining viable cells were maintained in 200 μM $ZnCl_2$ until the cells become confluent in about 20 days. The cells were plated at a density of 50,000 cells/well for 24 hours, and medium was changed at 24 hours and incubated for further 24 hours. The cells were then live stained with 10 nM Hoechst-33342 and imaged for counting nuclear shapes (Figure S1E).

Parallelly, zinc resistant cells were tested for C19MC miRNA expression after extracting RNAs, cDNA synthesis for miRs-519D, and 526B, and qRT-PCR (See below) (Figure S1E).

Quantitative real-time-PCRs (qRT-PCRs) and reverse transcriptase PCRs (RT-PCRs)

qRT-PCRs

Quantitative real-time PCRs were performed as described previously.[17] RNAs were isolated using miRNeasy Mini Kit, quantified, and 250 ng RNAs were subjected to cDNA synthesis using Multiscribe reverse transcriptase, RNAse inhibitor, 10X buffer, dNTPs, (TaqMan MicroRNA Reverse Transcription Kit: ABI, Cat # 4366596) and RT TaqMan Primers listed in key resources table titled "List of real-time qRT-PCR reagents used in this study". The cDNAs were subjected to qRT-PCR reactions using corresponding primers with probes and Taqman master mix listed in key resources table titled "List of real-time qRT-PCR reagents used in this study".

Comparative Ct (ΔΔCt) method was used to calculate the relative expression of miRNAs compared to pMir controls or untransfected controls as appropriate, after normalizing the values based on RNU6B. The results were plotted using GraphPad Prism software as bar graphs with standard error of mean as error bars (v7.04; La Jolla, CA, USA).

RT-PCRs

For RT-PCRs, Total RNA was isolated using TRIZOL reagent as per manufacturer's instructions and the reactions were performed as described previously.[17] Briefly, 20 μl cDNA synthesis reactions were performed using 1 μg RNA and High-Capacity cDNA Reverse Transcription Kit. 1.5M final concentration of betaine (from 5M stock) was added to the cDNA reactions. The thermocycler conditions used were, 25°C for 10m, 37°C for 120m and 85°C for 5m. The cDNAs were diluted with 30 μl of nuclease free water before subjecting 2.5 μl cDNA to PCR reactions. For the PCR step, 1M betaine (final conc.) was used along with regular PCR reaction components. A list of primers used in RT-PCRs are specified in key resources table titled "List of custom PCR primers used in this study". The thermocycler conditions for all PCR reactions have an initial denaturation of 95°C for 5-minutes, cycling denaturing (95°C) time of 1-minute, annealing temperature of 60°C (30 seconds) and 1 minute of extension time (72°C), with 34 cycles. A final extension at 72°C was given for 5 minutes. The PCR reactions were run with GeneRuler 100 bp DNA Ladder using 2% agarose gels. The gels were imaged using LI-COR Odyssey Fc imager (Lincoln, NE, USA).

Nuclear coverage of mitochondria (NCoM) quantification and visualization in R

Mitochondria are known to have contact sites with various cytoplasmic organelles such as endoplasmic reticulum (ER) and nucleus. Mitochondria can have a wide-variety of distribution within cells such as perinuclear distribution. To understand the role of C19MC miRNAs in nuclear coverage of mitochondria (NCoM), we plated the CRISPR engineered WM793 cells (NGP and Choppers) in parallel to the parental cells at the density of 50,000 cells/ml in 6-well plates. At 24 hours, the cells were treated (not transfected) with 30 nM of Cy5-CSi000A RNA mitochondria probe in fresh MEM for further 24 hours. 30 minutes before the end of treatment duration, the cells were live stained with 10 nM Hoechst-33342 for imaging nucleus and mitochondria distribution using appropriate filters. Merged as well as individual channel images were exported and the 2D circumference coverage of nucleus (Hoechst-33342-positive DNA) by mitochondria were measured using ImageJ. Briefly, nuclear circumference (perimeter) was measured by drawing around the Hoechst-33342 positive DNA in addition to mitochondria signal (Cy5-CSi000A) overlapping perimeter of the nucleus. From these values the percentage of mitochondria covered nuclear perimeter was calculated for each cell. 100 such cells were measured for each cell type and the data were visualized in R using ggplot2[34] package as violin plots with standard error (orange lines) of mean (red line) (R version 4.1.3) (Figure 4H). Please see below for R-codes. Statistical significances were calculated in Microsoft Excel using t-test option.

Tracking the role of autophagy and CDK1 in nuclear coverage of mitochondria and mitochondrial load/cell

To examine the role of autophagy and CDK1 in regulating the nuclear coverage of mitochondria (NCoM), we used the WM793-CRISPR-NGP cells which have a predominant distribution of mitochondria at the perinuclear region. WM793-CRISPR-NGP cells were plated at a density of 50,000 cells/ml in 6-well plates (4ml cells/well). At 24 hours after plating, the cells were treated with 20 μM chloroquine (CQ) or with 10 μM CDK1 inhibitor Ro3306 for 24 hours. DMSO was used as vehicle control and chloroquine does not have a vehicle control as it was freshly dissolved in distilled water. The cells were live stained for Hoechst-33342, imaged and nuclear coverage of mitochondria measured as described above and the data were visualized in R using ggplot2[34] package as violin plots with standard error (orange lines) of mean (red line) (R version 4.1.3) (Figures 4H and 4I). Statistical significances were calculated in Microsoft Excel using t-test option.

R CODE

```
> ggplot(DFname, aes(x = Cells, y = NCoM)) +
    geom_violin(trim=FALSE, fill="grey90", color="black") +
    stat_summary(fun.data = "mean_cl_normal", geom = "errorbar", width = 0.15, linewidth = 1, colour = "orange")+
    stat_summary(fun = "mean",
       geom = "crossbar",
       width = 0.2,
       colour = "red")+
  theme_classic()
  # Axis limits were based on auto package settings.
```

Tracking the relative mitochondrial abundance/load per cell

Relative mitochondria abundance per cell were calculated from the CSi000A signal/cell after normalizing the data to fix the control averages to 100 % so that the variations between treatment conditions can be inferred in terms of percentage change (Figure 4I). The data were plotted in GraphPad Prism using aligned dot plot with standard error of mean and 75 % transparency settings for data points. Statistical significances were calculated in Microsoft Excel using t-test option.

TCGA H&E diagnostic slides/histology

C19MC^{High} histology diagnostic slides were downloaded from GDC web portal https://portal.gdc.cancer.gov/ by feeding in the TCGA de-identified IDs of C19MC^{High} patients. The slide images were examined using Aperio ImageScope software at maximum magnification. When pathologist's mark is available, the presence or absence of nucle(ol)ar invasive cytoplasm and meiotic nuclear division in cancer cells were examined within the mark. The C19MC^{High} histology with nucle(ol)ar invasive cytoplasm and meiotic nuclear division qualitatively falls under embryonal carcinoma histology regions within the whole slide images and were prominent in TGCTs than any cancer type correlating to the GSEA signatures that were high in TGCTs than in any other C19MC^{High} cancer types. Sickle nuclei were restricted to few cancer types (please see main text) despite sickle-like nuclei with slender and curvy nuclei were observed in multiple C19MC^{High} cancers with teratoma histology (and were not considered as sickle nuclei). Sickle nuclei with signet-ring carcinoma like morphology were also not considered as meiotic sickle nuclei, as in those signet-ring cells the sickle nuclei are potentially due to a large vacuole-like region that occupy the concave side of the curved nuclei and that could be mucin-filled bags or lipid drops that got lost during H&E preparation by organic solvents. Therefore, only sickle nuclei with condensed chromosomes on the concave side of the nuclei (Figure S1B) or with embryonic nuclear division (END) (Figure S1J) were considered meiotic sickle nuclei. Finally, meiotic nucle(ol)ar invasive cytoplasm and meiotic nuclear division are readily distinguishable from mitotic cells with lagging chromosomes (Figure S4D vs. E).

Nuclear margination of chromatin and mitochondria in living cells

MCF-7 cells were plated at 50,000 cells/ml in complete MEM for 24 hours and treated with Aurora-B inhibitor (AZD1152-HQPA) (20 nM) and Cy5-CSi000A (30 nM) for 24 hours and then the cells were subjected to 10 nM Hoechst-33342 nuclear DNA staining as described previously.[6,45] The cells with meiotic nuclear division were imaged to show that the Hoechst-33342-positive DNA is marginated along the nuclear periphery (Figure S4C) similar to meiotic nuclear division *in vivo* in multiple C19MC^{High} cancer types (Figure S4D). Notably, the mitochondria too aligned with the nuclear margin (Figure S4C).

Softwares, packages, web-servers used and figure compositing

A list of softwares used in this study are listed in key resources table titled "List of softwares/packages/web servers used in this study". All graphs, plots, images exported from respective softwares were finally composited in Adobe Photoshop CS5 while keeping main plot area original but replacing axis fonts to have a uniform font size. Labeling, gate (dotted) lines were introduced in Photoshop while corresponding data analysis with respect to the gated lines were done in original softwares such as GraphPad Prism or in Microsoft Excel. TCGA histology slides were opened in Aperio ImageScope software at maximum magnification and were transferred to photoshop cache or to Microsoft Paint, through Windows 10 print screen shot snippet before being composited. Certain graphical schematic elements such as chromosomes (Figures S2D and S2H) and nuclei with bridge, sliced mitochondria (in Figure S4B) etc., were modelled and rendered in Lightwave-3D software and imported to Adobe Photoshop composite. Certain elements were added to the microscope image to mark the boundary of cells (Figure 2H green lines) and Figure S1B (Black lines). Arrows, arrow heads, scale bar lines of magnification of microscope images were also added using Photoshop in the composite, where the scale bars are based on original microscope image scale bars.

QUANTIFICATION AND STATISTICAL ANALYSES

Quantification of immunofluorescence intensity per cell or subcellular location such as nucleus or NiC, mitochondrial coverage of nucleus etc., were done using ImageJ software and are discussed in appropriate sections above.

Statistical analyses (unpaired, nonparametric, Mann-Whitney test) for pan-cancer C19MC^{High} versus C19MC^{Low} groups were performed using GraphPad Prism software (v7.04; La Jolla, CA, USA). These analyses were also done between normal versus tumor samples but has a downside of lacking normal controls for multiple cancer types. The cumulative C19MC expression data were plotted as aligned dot plot with SEM and that data points with a transparency of 50-75%. For *in vitro* experiments, two-tailed, two-sample unequal variation-based t-test was performed to calculate statistical significance in Microsoft Excel 2010 or 2021 and the graphs were plotted either in excel or in GraphPad Prism software. The p-values were indicated directly within figure panels. All *in vitro* experiments were done with at least 3 replicates and in case of chromosome counts a minimum of 25 spreads instead of standard 10 spreads were counted. Experiments were repeated at different timelines to make sure reproducibility of key findings. For most individual cell measurements [for example, nucle(ol)ar invasive cytoplasm (NiC) size measurement], 300 cells were measured from replicates and were pooled to have comparisons with individual cell types or treatment conditions and to have the overall range of variability. More details on statistics and graph settings and codes using statistics within R packages such as ggplot2 were given in appropriate sections above. Results with borderline significances (p-value close to 0.05) were omitted or not chased further. Unless the non-significance is relevant to show that the vehicles are not doing the phenotypic changes, the experiments with insignificant results were not included.